

# Superconducting theory of polyhedral quantum confined electrons

Xiuqing Huang<sup>1,2\*</sup>

<sup>1</sup>*Department of Telecommunications Engineering ICE, Army Engineering University, Nanjing 210007, China*

<sup>2</sup>*National Laboratory of Solid State Microstructures, Nanjing University, Nanjing, 210093, China*

(Dated: June 9, 2024)

Based on experimental evidence from scanning tunneling microscopy and spectroscopy, angle-resolved photoemission spectroscopy, and neutron scattering in high-temperature superconductors, we present a unified theoretical framework that the confined electrons within polyhedral quantum wells as the Mott ground state and the symmetry-breaking of electron-proton pair as the superconducting mechanism. The new theory enables the analytical determination of fundamental properties in copper- and iron-based superconductors. These properties include the magic doping and checkerboard charge order, Fermi surface structure and its splitting, the symmetry and value of the superconducting energy gap, the superconducting transition temperature, and the spin resonance peaks and their parity. The theoretical predictions of our model show strong agreement with experimental findings. Moreover, our research offers novel insights into the microscopic nature of magnetism, spin, holes, localized Cooper pair, magnetic monopoles, the Ginzburg-Landau order parameter, and the Meissner effect.

PACS numbers: 74.20. -z, 74.25.Ha, 75.10. -b

## I. INTRODUCTION

The discovery of superconductivity by Onnes in 1911 marked a significant milestone in physics<sup>1</sup>. Several decades later, the BCS theory provided an explanation for superconductivity, attributing it to the formation of Cooper pairs through electron-phonon interactions<sup>2</sup>. However, the emergence of high-temperature superconductors (HTS), including both copper-<sup>3-6</sup> and iron-based materials<sup>7-11</sup>, presented a formidable challenge to existing theories and sparked intensive investigations into the unique properties and underlying mechanisms of these compounds. Several microscopic theories and models, such as the RVB<sup>12</sup>, Hubbard models<sup>13</sup>, gauge theory<sup>14</sup>, spin singlet<sup>15</sup>, amperian pairing<sup>16</sup>, and d-wave pairing<sup>17-19</sup>, have been proposed. While these theories may capture certain superconductivity aspects, they have yet to be deemed entirely satisfactory<sup>20</sup>.

Scanning tunneling microscopy and spectroscopy (STM and STS)<sup>21-24</sup>, angle-resolved photoemission spectroscopy (ARPES)<sup>25,26</sup>, and neutron scattering techniques<sup>27</sup> have emerged as powerful tools for investigating the electronic and magnetic properties of materials. These advanced experimental techniques help researchers to obtain visual information about the real-space structure of electronic states, electronic band structure, Fermi surface topology, energy gaps, and magnetic excitations in HTS. Physicists constructed an intricate phase diagram of cuprate superconductors by analyzing these experimental data<sup>28</sup>. This phase diagram reveals the existence of various electronic phases, including pseudogaps<sup>29</sup>, antiferromagnetic phases<sup>30</sup>, stripe-like structures<sup>21,31,32</sup>, charge density waves (CDW)<sup>22,33</sup>, spin density waves (SDW)<sup>34,35</sup>, nematic states<sup>36,37</sup>, magic doping states<sup>38,39</sup>, pair density waves (PDW)<sup>40,41</sup>, and others. Despite decades of extensive research, the microscopic mechanisms underlying high-temperature superconductivity still need to be better understood<sup>42,43</sup>.

HTS are considered to be strongly correlated systems; numerous STM experiments have demonstrated that the free electrons within superconductors are not truly free. Instead,

they tend to form orderly commensurate or incommensurate local charge stripe phases<sup>43-46</sup>, especially when the concentration at the so-called magic doping  $x = 1/8$ , the stable  $4a_0 \times 4a_0$  Wigner crystal with checkerboard patterns is widely observed<sup>23,38,47-55</sup>. Furthermore, many reports suggest that the Cooper pairs can form and be localized in real space<sup>56-58</sup>. Recent STS experiments also provided strong evidence supporting the idea that doped holes may be locally paired within the charge stripes in real space<sup>59</sup>. Since high-temperature superconductivity is achieved through disorderly doping in a pure Mott insulator<sup>60</sup>, it appears that the presence of impurities enhances the likelihood of achieving zero-resistance superconductivity. This observation contradicts Anderson's theory of localization<sup>61</sup>, which suggests that increased disorder leads to highly resistive localized states rather than the zero-resistance superconducting state. Moreover, the discovery of locally paired Cooper pairs in real space challenges the hypothesis of delocalized Cooper pairs in momentum space proposed by the BCS theory of phonon-mediated<sup>62</sup>. The most recent research directly shook the physical foundation of the necessity of electron pairing as the superconducting mechanism<sup>63</sup>.

Angle-resolved photoelectron spectroscopy instruments can be likened to cameras in that they capture and record information to ascertain the physical characteristics of the objects being measured. Thus, the target object should remain stationary for a clear measurement image. Experimental findings have shown that different superconducting materials display unique characteristic energy spectrum structures, capable of reflecting even subtle changes in carrier concentration<sup>25,64-70</sup>. However, accurately interpreting experimental data presents a significant challenge, as the measured object acts as a 'black-box'. Moreover, the uncertainty introduced by the external energy applied during detection can potentially obscure the true nature of the electronic state. To accurately interpret ARPES experimental outcomes for copper-based and iron-based superconductors, it is essential to recognize their nature as strongly correlated systems. Within these systems, electrons' kinetic energy

is markedly lower than the local Coulomb potential energy. This leads to a pivotal question: Is the experimental data observed chiefly indicative of the electrons' dynamic kinetic energy, or does it reveal the static Coulomb potential energy as delineated by the Fermi surface?

Neutron scattering is a valuable technique that provides crucial insights into superconductors by investigating magnetic ordering, spin correlations, and spin fluctuations through the utilization of magnetic interactions<sup>71-73</sup>. Conversely, superconducting materials exhibit zero resistance in the presence of an electric field and display the Meissner effect when subjected to a magnetic field<sup>74</sup>. Both of these phenomena are intimately connected to the magnetic field, as described by Ampere's law. The interpretation and utilization of these experimental observations to establish a comprehensive theory of superconductivity raise a fundamental yet unresolved question: What is the true nature of magnetism<sup>75</sup>?

It is widely recognized that many theories of superconductivity draw upon the Drude quasi-free electron model<sup>76</sup>. This model posits that the valence electrons within a superconductor are in constant motion in both the normal and superconducting states. Within this framework, a primary challenge in the theory of superconductivity is to elucidate how electrons manage to avoid collisions with the lattice and pair up, leading to zero electrical resistance<sup>2</sup>. However, the superconductivity research community has primarily overlooked an essential scientific aspect. It is well known that electrons emit photons and lose energy during the transition process due to the non-uniform electric field inside atoms. Similarly, the non-uniform lattice Coulomb field within superconductors inevitably leads to electrons' non-inertial, variable-speed motion. This raises a critical question: How do electrons avoid emitting electromagnetic waves and thereby avoid energy loss in such a scenario? Furthermore, it contradicts a fundamental principle of thermodynamics to assume that electrons moving randomly can spontaneously condense into superconducting states without any energy loss, merely through pairing coherence.

So far, another puzzling question remains for researchers: Despite extensive theoretical deductions and complex numerical calculations, why does the current theoretical model of superconductivity fail to explain high-temperature superconductivity? We argue that all existing models violate basic physical facts, so they cannot explain any superconductor. Taking the Hubbard model as an example<sup>13,77</sup>, the Hubbard Hamiltonian is written as:

$$\hat{H} = -t \sum_{\langle ij \rangle \sigma} c_{i\sigma}^+ c_{j\sigma} + U \sum_i c_{i\uparrow}^+ c_{i\downarrow}^+ c_{i\uparrow} c_{i\downarrow},$$

where the constant hopping term  $t$  is the tight binding kinetic energy. This simplification of assuming inertial electrons that consume no energy during hopping implies a lossless process. However, considering the unavoidable electromagnetic energy losses mentioned earlier, this assumption of lossless electron hopping in a quantized model is physically unrealistic. If electrons continuously hop within the lattice, the hopping term must vary in time and space.

Such a Hamiltonian is inherently unsolvable and cannot accurately describe the phenomenon of zero-resistance superconductivity. Alternatively, another possibility is that electrons are localized, meaning that the kinetic energy  $t$  of the above Hamiltonian is zero.

The ancient Chinese philosopher once said: The great way is extremely simple. Motion and stillness are fundamentally distinct physical forms (Dynamics and Statics). Electron motion encompasses infinite uncertain and unstable states, while stillness represents the sole definitive stable state. The collective motion of a large number of electrons inevitably entails phenomena such as dispersion, diffusion, collisions, and dissipation. The introduction of quasi-particles, exemplified by phonons, not only fails to prevent the occurrence of these phenomena but further amplifies the degree of uncertainty. On the contrary, the hypothesis of localized electrons can circumvent all these issues, rendering so-called challenges like electron-electron and electron-lattice collisions nonexistent. Of course, there is no longer a need to find the 'glue' that binds electrons into Cooper pairs<sup>20</sup>. Under the simple paradigm of local electrons, the existing challenge is how the electrons generate current. We argue that the symmetry breaking caused by the small directional displacement of electrons in the equilibrium position can generate current.

Symmetry and symmetry breaking are fundamental principles in modern physics. When the symmetry of a system is broken, new physical quantities and phase transitions can emerge. What is the relationship between broken physical quantities and structures? This question has sparked a debate between reductionism and emergentism. When a superconductor enters the superconducting state, a steady magnetic field can be measured around it, the reductionism suggesting the presence of perpetual electron motion and undecaying supercurrents within the material. Similarly, the concept of electron spin arises from experimental observations of magnetism in specific environments, and reductionism posits that electrons possess an intrinsic spin. Is deterministic reductionism correct? As Anderson pointed out in the well-known article *More is Different*<sup>78</sup>, the emergent phenomena that microscopic electrons are more likely to show is not simply as one plus one equals two. For example, when electrons and protons combine, they can form not only neutrons and hydrogen atoms but also behave as Plank's quantized harmonic oscillators, emitting quantized photons. We will show that the electron-proton pairing can function as electric dipoles, capacitors, and magnetic monopole pairs, contributing to the order parameter, current, and magnetic field.

In this paper, we leverage a comprehensive array of experimental results from STM, STS, ARPES, and neutron scattering studies on copper- and iron-based superconductors to underscore the need for new paradigms to investigate superconducting mechanisms. Based on these findings, we propose a unified microscopic mechanism rooted in Mott insulators with localized electrons. Within this framework, we ascribe currents and magnetic fields to Maxwell displacement currents and Dirac magnetic monopoles instead

of traditional electron motion. Our research offers valuable insights into the unique behaviors of these materials and successfully formulates a single, self-consistent theory of superconductivity applicable to all superconductors. Through this novel theoretical lens, we offer a consistent and comprehensive definition for the microscopic nature of magnetism, spin<sup>79</sup>, hole, magnetic monopole<sup>80</sup>, Cooper pair, and the Ginzburg-Landau order parameter<sup>81</sup>, effectively explaining their interrelationships. Furthermore, the new mechanism offers a fresh understanding and explanation of the microscopic physical essence behind the zero electrical resistance and the Meissner effect in superconductivity.

## II. CU-BASED SUPERCONDUCTORS

The discovery of cuprate superconductors has revealed that superconductivity can manifest at temperatures much higher than what was anticipated by the BCS theory. This breakthrough underscores the need for a more comprehensive theory of superconductivity capable of explaining the unique properties observed in these materials. A growing body of experiments indicates that pairing interactions might be predominantly localized. As a result, the concept of local pairing holds promise in unraveling the intricacies of high-temperature superconductivity.

### A. Localized Cooper pair and checkerboard phases

There are two distinct models for describing the behavior of electrons within solid materials: (1) the Drude model<sup>76</sup>, in which electrons are almost unaffected by the local lattice potential and can move freely within conductors and superconductors; (2) the Planck model<sup>82</sup>, which treats electrons as quantized energy oscillators that are confined to localized potential wells within the lattice, undergoing thermal vibrations at higher temperatures. As a question, which model better aligns with the actual microphysical world?

The two recent experiments may address this question. The first experiment, conducted using ARPES on overdoped Bi2212 samples, revealed Cooper pairs well above the critical temperature<sup>83</sup>. The second experiment, performed using STS on extremely underdoped  $\text{Bi}_2\text{Sr}_{2-x}\text{La}_x\text{CuO}_{6+\delta}$  samples<sup>59</sup>, confirmed that Cooper pairs are spatially localized in real space. Combining these findings leads to the conclusion that the localization of electrons (or Cooper pairs) is an intrinsic self-organizing behavior. Disorder and temperature can only perturb the vibrational energy of electrons to a limited extent. Therefore, the physical basis for Planck's quantization hypothesis lies in the localization of electrons.

Fig. 1a shows the undoped  $\text{Bi}_2\text{Sr}_2\text{CuO}_{6+\delta}$  (BSCO) single cell in the insulating phase, due to the strong Coulomb confinement from the surrounding lattice ions, the electron becomes localized within a quantum well with an octahedral shape. Without an external field, these electrons are trapped inside the quantum wells and cannot escape to become free

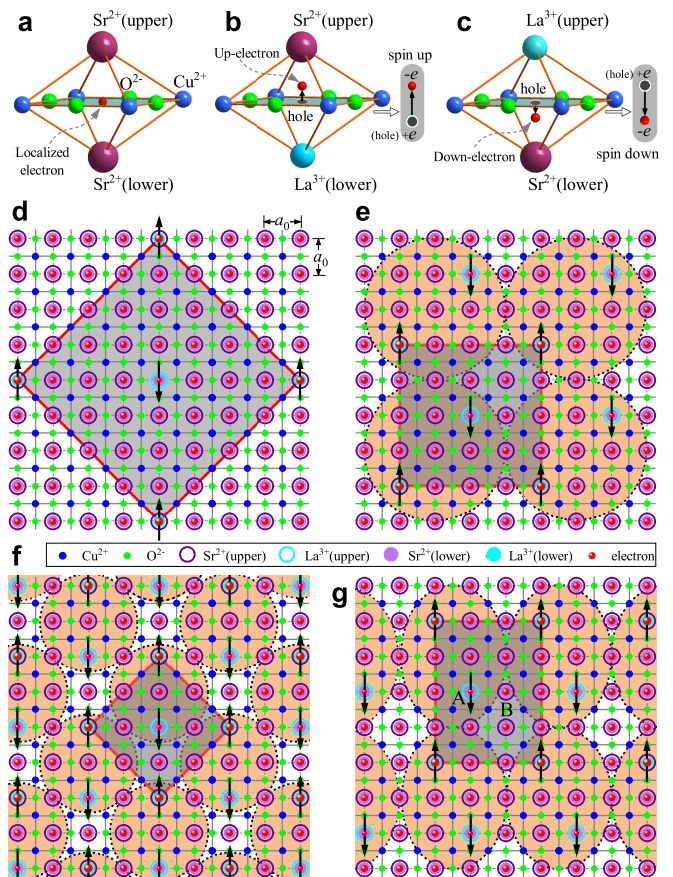


FIG. 1. Localized Cooper pairs and electronic state structures in real space of copper oxide superconductors. **a** Octahedral quantum well and localized electrons in cuprate BSCO. **b** and **c** Doping-induced symmetry breaking and the emergence of holes and spins (electric dipoles). **d** – **g** doping level and the real-space charge ordering, **d** – **f** the magic doping levels at  $x = 1/16$ ,  $1/8$ , and  $1/4$ , with  $4\sqrt{2}a_0 \times 4\sqrt{2}a_0$ ,  $4a_0 \times 4a_0$ , and  $2\sqrt{2}a_0 \times 2\sqrt{2}a_0$  checkerboard-like structure, respectively; **g** the optimal doping of  $x = 1/6$  resulting in a nematic charge order. An up-electron (**b**) and a down-electron (**c**) can pair up to form quantized real-space Cooper pairs.

electrons. When lanthanum is doped, the  $\text{La}^{3+}$  substitutes the  $\text{Sr}^{2+}$  in two ways. In doping at the lower position (Fig. 1b), the electron is pushed upward away from the  $\text{CuO}_2$  plane and rests at a new equilibrium position as the up-electron, leaving behind a hole at its original location. In the way of doping at the upper position (Fig. 1c), the electron is pushed downward away from the  $\text{CuO}_2$  plane as the down-electron, and the original location also forms a hole. Fig. 1a is symmetric, with the centers of positive and negative ions overlapping perfectly. Doping leads to symmetry breaking, as shown in the right inset of Figs. 1b and c, which are equivalent to generating upward and downward unit electric dipoles (or spin-up and spin-down), respectively. As well known, a Cooper pair consists of two electrons with opposite momenta and opposite spins. By analogy, we use  $\mathbf{k}$  and  $-\mathbf{k}$  to represent the upward and downward displacements of the electrons in Figs. 1b and c, respectively, and  $\uparrow$  and  $\downarrow$  to

represent the up and down orientations of the electric dipoles. Then, the electronic states in Figs. 1b and c can be denoted by  $|\mathbf{k}\uparrow\rangle$  and  $|\mathbf{k}\downarrow\rangle$ , respectively, and their combination can be defined as a real-space localized Cooper pair.

One of the most incredible phenomena of high-temperature superconductors is that a minimal change in doping concentration can manipulate the phase transition between insulating and superconducting phases. How doping induced the evolution of superconductivity is an open problem that the existing superconducting theory and mechanism can not explain. Here, we show how doping changes the electronic structure within  $\text{CuO}_2$ . Figs. 1d–g depicts a top view of the (Sr/La)-(CuO)-(Sr/La) sandwich quasi-two-dimensional structure, representing four different doping samples. Figs. 1d–f correspond to the magic doping levels  $x=1/16$ ,  $1/8$ , and  $1/4$ <sup>39,84–86</sup>, respectively. These three samples have rational doping and exhibit electronic structures as a checkerboard pattern of  $4\sqrt{2}a_0 \times 4\sqrt{2}a_0$ ,  $4a_0 \times 4a_0$ , and  $2\sqrt{2}a_0 \times 2\sqrt{2}a_0$ , respectively. These figures show that the up-electrons of Fig. 1b always appear paired with the down-electrons of Fig. 1c. For the sake of intuition, we can recombine the electronic structure with local Cooper pairs with diameters of  $4a_0$  and  $2\sqrt{2}a_0$  (see Figs. 1e and f). Because the symmetry of the electronic structures is consistent with the symmetry of the  $\text{CuO}_2$  plane, all electrons in the magic doping samples are pinned to their equilibrium positions and cannot move. Therefore, these three doped superconducting materials still behave as insulators.

Fig. 1g represents the case of  $x = 1/6$  of optimal doping, a sample where  $x$  is an irrational number. Compared with the quadruple symmetry of the  $\text{CuO}_2$  plane, where the electronic structure undergoes symmetry breaking. Even though the up-electrons form a nematic state with a  $3a_0 \times 4a_0$  pattern, there is uncertainty in the staggering center position of the down-electrons (denoted as A or B in the figure). Due to the mismatch between electronic structure and lattice symmetry, electrons' localization and pinning strength are reduced. When an external field is applied, the electrons will deviate from the equilibrium position and have a small directional displacement, thus generating a displacement current. Therefore, the essence of supercurrent is displacement current rather than the motion of electrons as in conventional conduction currents. A more detailed discussion will follow in a later section.

Before concluding this section, it is necessary to highlight the importance of symmetry breaking in studying the mechanism of superconductivity. Modern physics proposes electron spin based on the atomic fine spectral structure and the Stern-Gerlach silver atomic beam experiment<sup>79</sup>. However, these experiments only demonstrate magnetic moments in atoms such as silver or hydrogen, not free electrons. We argue that the naked electrons do not possess the property of spin; instead, the magnetic properties of electrons originate from the symmetry breaking of the surrounding ion lattice. Taking the above Figure as an example, the electron does not show spin in Fig. 1a, as no symmetry breaking occurs. In Fig. 1b and c, the electrons are assigned up- and down-spins due to upward and downward symmetry breaking.

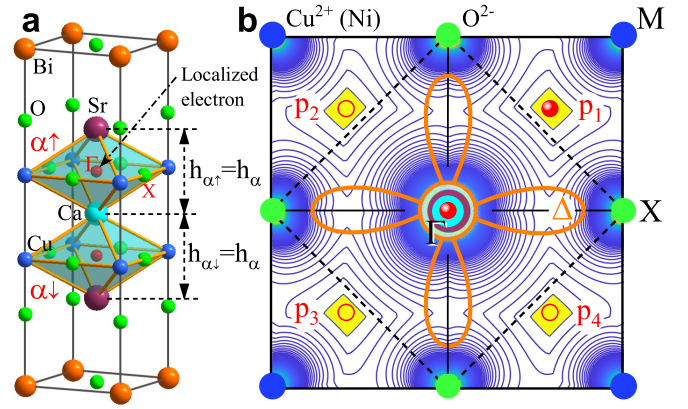


FIG. 2. The physical origin of d-wave symmetry of copper-based superconductors. **a** Octahedral cages (quantum well) and localized electrons in cuprate Bi2212; **b** Four real space pockets of electrons and d-wave symmetry in a unit cell of  $\text{CuO}_2$  plane.

## B. D-wave symmetry and $T_c$

An essential feature of the superconducting state in copper oxide is its d-wave symmetry, which is considered the key to solving the mechanism of high temperature superconductivity. Since the high-quality  $\text{Bi}_2\text{Sr}_2\text{CaCu}_2\text{O}_{8+\delta}$  (Bi2212) single crystal samples within a relatively wide range of doping levels can be prepared at the laboratory level and it is easy to cleave to get smooth sample surface for ARPES measurements, the Bi2212 superconductor has been intense studied by ARPES<sup>50</sup>. Unlike Fig. 1a, in Fig. 2a, a pair of oppositely oriented octahedral structures act like conjoined twin cages, trapping a pair of localized electrons.

Figure 2b presents a numerical simulation of the electromagnetic force exerted by confined electrons on one of the  $\text{CuO}_2$  surfaces within the octahedron. Two types of electrons can exist: the central  $\Gamma$ -electrons and the  $p$ -electrons located in the four yellow pockets. The material's superconducting properties are determined by the ground state  $\Gamma$ -electrons, which experience the strongest Coulomb confinement inside the center of the octahedron. The excited state  $p$ -electrons, with weaker constraints, can easily escape the confinement of the octahedron and become photoelectrons when they acquire photon energy. In ARPES experiments<sup>87,88</sup>, these photoelectrons accumulate over time to form Fermi arcs or Fermi pockets. When  $T < T_c$ , the  $p$ -electrons can return to the ground state and become superconducting  $\Gamma$ -electrons. However, when  $T > T_c$ , under the Coulomb attraction of the copper ions (M), the  $\Gamma$ -electrons transition to the excited state in the diagonal direction (nodal) as  $p$ -electrons, while in the horizontal and vertical directions (X), they form large energy gaps due to the Coulomb repulsion of oxygen ions. Therefore, it should be clear that the pseudogap and d-wave symmetry are the result of the electromagnetic interaction between the localized electron in a single unit cell of the  $\text{CuO}_2$  plane and copper oxide ions around it and have no direct relationship with the superconducting mechanism.

For the recently discovered nickel-based high-temperature superconductor  $\text{La}_3\text{Ni}_2\text{O}_7$ <sup>89</sup>, under pressure, it undergoes a structural phase transition from AMAM to FMMM, forming octahedral quantum wells similar to copper-based superconductors, with  $\text{La}^{3+}$  ions as vertices and  $\text{NiO}_2$  as the confinement layer. Therefore, it is easy to predict that nickel-based superconductors have similar d-wave symmetry as Fig. 2b. The following section will further explore the relationship between quantum well structures and Fermi surface structures in different superconductors. These studies further indicate that the physical essence of the Fermi surface is the static electric field generated jointly by all ions within the crystal unit cell. There is no scientific basis for distinguishing conventional and unconventional superconductors based on energy gap symmetry or superconductivity transition temperature. All superconductors should have the same superconducting mechanism: the symmetry breaking of the condensed state of electrons.

The relationship between crystal structure and superconducting transition temperature is crucial in superconductor research. It has been found that  $T_c$  can be influenced by a range of factors, including the application of pressure and the substitution of elements (chemical pressure) with varying ionic radii. An important question arises: Among the physical parameters inherent to superconducting crystal structures, which one has the most significant correlation with  $T_c$ ? As shown in Fig. 2a, Bi2212 exhibits two degenerate octahedra with corresponding electron states of opposite orientations. We can use the distance  $h_\alpha$  between the two vertices of the octahedron to characterize the degree of electron confinement. The smaller the  $h_\alpha$  value, the stronger the electron confinement and the stronger the association between the  $\Gamma$ -electron and the octahedron. Consequently, the superconducting gap increases, and the superconducting transition temperature increases. The data in Table I can easily verify this conclusion. The table shows that there are usually two sets of different octahedra in copper-based superconductors, corresponding to the  $\alpha$  and  $\beta$  superconducting phases. Under applied pressure, the low-temperature superconducting  $\beta$  phase with big  $h_\beta$  may transition to the high-temperature superconducting  $\alpha$  phase with small  $h_\alpha$ . This issue will be discussed in detail later. Based on the statistical data in Table I, the relationship between the superconducting gap  $\Delta$ , the superconducting transition temperature  $T_c$ , and  $h = h_{\alpha(\beta)}$  is as follows:

$$\Delta \propto T_c = \frac{\bar{\lambda}_{Cu}}{h^2} \simeq \frac{1320}{h^2}. \quad (1)$$

Comparing the charge symmetry of  $\text{CuO}_2$  and  $\text{NiO}_2$  in Fig. 2b, it is found that copper-based and nickel-based superconductors are identical, so the above formula also applies to nickel-based superconductors. As we know, the  $\text{La}_3\text{Ni}_2\text{O}_7$  single crystal sample reaches about 80 K at a pressure exceeding 14 GPa. The most recent theoretical studies suggest that  $\text{Tb}_3\text{Ni}_2\text{O}_7$  is an interesting candidate for superconductivity under ambient pressure<sup>90</sup>. Therefore, it raises an interesting question: Will the

TABLE I. The relationship between  $T_c$  of copper-based superconductors and the distance  $h$  between two vertices of octahedral quantum well,  $h = h_\alpha$  (or  $h_\beta$ ), where  $\lambda_{Cu} = T_c h^2$ . The values in bold are possible superconducting phases.

Compound	$T_c$ (K)	$h_\alpha$ (Å)	$h_\beta$ (Å)	$\lambda_{Cu}$
$YBa_2Cu_3O_{7-\delta}$	93	<b>3.6720</b>		1254
$Bi_2Sr_2Ca_2Cu_3O_{10+\delta}$	110	3.1511	<b>3.3272</b>	1217
$TlBa_2CaCu_2O_{7+\delta}$	103	<b>3.5771</b>		1317
$TlBa_2Ca_3Cu_4O_{11+\delta}$	112	3.2453	<b>3.5025</b>	1373
$TlBa_2Ca_2Cu_3O_{10+\delta}$	120	<b>3.2381</b>	3.5305	1258
$Tl_2Ba_2Ca_2Cu_3O_{10+\delta}$	128	<b>3.3053</b>	3.5252	1393
$HgBa_2CuO_{4+\delta}$	94	<b>3.8241</b>		1374
$HgBa_2Ca_2Cu_3O_{8+\delta}$	134	<b>3.2108</b>	3.4241	1380

highest transition temperature of Ni-based superconductors exceed that of Cu-based superconductors? Based on the experimental data provided in the paper<sup>89</sup>, the value of  $h = (0.5 - 0.316) \times 19.734 = 3.631$  Å. By substituting this value into Eq. (1), the highest superconducting transition temperature  $T_c(max)$  of Ni-based superconductors can be estimated at 100 K. Hence, it is unrealistic to think that the  $T_c$  of Ni-based superconductors can surpass that of Cu-based superconductors and even realize room-temperature superconductivity.

It is necessary to emphasize that the commonly accepted academic viewpoint that better conductivity leads to easier achievement of superconductivity needs to be corrected. Conductivity and superconductivity are usually contradictory to each other. As is well-known, the best conductors, like gold, silver, and copper, are not superconductors; conversely, high-temperature superconductors usually originate from insulators. The essence of the pressure effect is to increase electron localization, which confirms that stronger electron localization is more likely to achieve higher-temperature superconductivity, as illustrated by Eq. (1).

### C. Bilayer-split Fermi surface Sheets in Bi2212

Fig. 2a shows that a pair of twinned octahedra ( $\alpha \uparrow$  and  $\alpha \downarrow$ ) connected by calcium (Ca) can be constructed in the Bi2212 unit cell, with each octahedron corresponding to a set of Fermi surface sheets (Fermi arcs). Under low doping conditions, the octahedra do not undergo distortion, and  $h_\alpha = h_{\alpha\uparrow} = h_{\alpha\downarrow}$ , as shown by the dotted line in Figs. 3a and b. Hence, in ARPES experiments, a doubly degenerate Fermi arc indicated by the red line in Fig. 3c can be observed.

In the case of heavy overdoped, an uneven distribution of dopants can occur in the upper and lower octahedra<sup>91</sup>, leading to the occurrence of the Jahn-Teller effect and causing distortion of the octahedra. In the overdoped  $\text{CuO}_2$  plane ( $p = 0.27$ ), the stretching deformation ( $h_{\alpha\uparrow}$  to  $h_{\alpha\uparrow}$  in Fig. 3a) of the confined octahedron, results in a localized antibonding electronic state. In the underdoped  $\text{CuO}_2$  plane ( $p = 0.14$ ), the contraction deformation ( $h_{\alpha\downarrow}$  to  $h_{\alpha\downarrow}$  in Fig. 3b) of the octahedron leads to a localized bonding electronic state.

In our theoretical framework, the Fermi surface structure

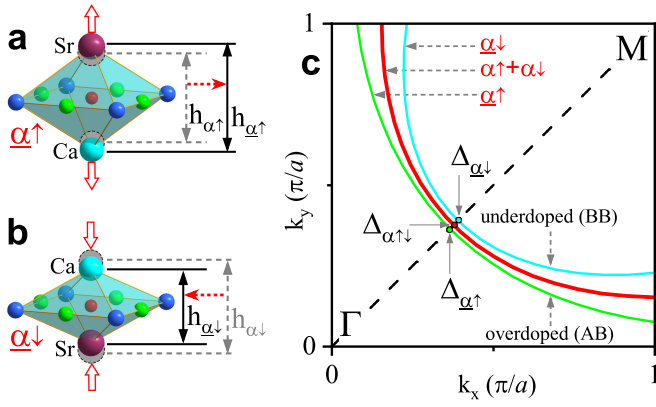


FIG. 3. Fermi surface bilayer-splitting induced by Jahn-Teller effect in Bi2212. **a** In the overdoped  $\text{CuO}_2$  plane, the stretching deformation of the confined octahedron, results in a localized antibonding electronic state. **b** In the underdoped  $\text{CuO}_2$  plane, the contraction deformation of the octahedron leads to a localized bonding electronic state. **c** the main red degenerate Fermi arc splits into the green antibonding Fermi sheet (AB) for overdoped  $\text{CuO}_2$  plane, and the cyan bonding Fermi sheet (BB) for underdoped  $\text{CuO}_2$  plane, respectively.

is determined by the contribution of  $p$ -electrons within the  $\text{CuO}_2$  unit cell pocket (Fig. 2b). Qualitatively, since  $h_{\alpha\uparrow} > h_{\alpha\uparrow\downarrow} > h_{\alpha\downarrow}$  (see Figs. 3a and b), the binding energy of the  $p$ -electrons with the three different octahedra satisfies:  $E_B^{\alpha\uparrow} < E_B^{\alpha\uparrow\downarrow} < E_B^{\alpha\downarrow}$ . This implies that in the heavily overdoped Bi2212 superconductor, the heterogeneous doping leads to the presence of two distinct new energy states of  $p$ -electrons, which can be distinguished in ARPES experiments by the Fermi arcs with different energy gaps. Taking the diagonal direction as an example, as the energy gap is proportional to the binding energy, we have  $\Delta_{\alpha\uparrow} < \Delta_{\alpha\uparrow\downarrow} < \Delta_{\alpha\downarrow}$ . Consequently, experimental observations reveal that the green Fermi arc shifts along the MG direction and expands outward at both ends, while the cyan-colored Fermi arc deviates along the GM direction and bends inwardly at both ends, as shown in Fig. 3c. Surprisingly, the theoretical analysis based on the localized electrons in the octahedra aligns perfectly with the high-resolution laser-ARPES measurements<sup>91</sup>.

#### D. Fermi surface Sheets and abnormal $T_c$ in Bi2223

It has been found that the maximum  $T_c$  value of cuprate superconductors is highly dependent on the number of  $\text{CuO}_2$  planes within a structural unit and usually reaches the maximum at three layers. In the case of a three-layer  $\text{Bi}_2\text{Sr}_2\text{Ca}_2\text{Cu}_3\text{O}_{10+\delta}$  (Bi2223) superconductor, two unusual behaviors have been identified: (1) In ARPES measurements of the Bi2223 superconductor, the majority of observations reveal one or two Fermi surface sheets<sup>92-95</sup>. However, a recent report has indicated the presence of three Fermi surface sheets in Bi2223 superconductor<sup>96</sup>, (2) its  $T_c$  remains nearly constant in the optimal and over-doped regions, whereas

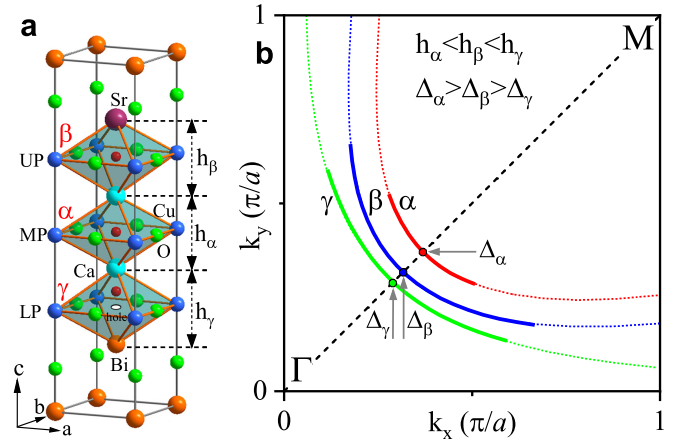


FIG. 4. The relationship between quantum confinement effects and the Fermi arc in Bi2223 superconductors. **a** Three octahedral quantum wells and their corresponding real-space localized electronic states ( $\alpha$ ,  $\beta$ ,  $\gamma$ ). **b** Three split Fermi arcs correspond to the three kinds of confined electrons.

most superconductors experience a decrease in  $T_c$  with increasing doping in the over-doped regions<sup>97</sup>. Researchers investigated using a  $6 \times 6$  Hamiltonian with 36 matrix elements to uncover the microscopic mechanism behind these two peculiar effects<sup>95,96</sup>. While it is possible to numerically fit the Fermi surface structure to match the experimental results by adjusting the parameters of the Hamiltonian, we believe that it is doubtful to capture the essence of the problem only through complex mathematical tools and computer simulation, and the way to obtain the truth should be much simpler.

Next, we use the local electron hypothesis to explain these two phenomena in a unified way. As shown in Fig. 4a, there are three possible octahedral quantum wells in the Bi2223 superconductor:  $\alpha$  in the middle layer,  $\beta$  in the upper layer, and  $\gamma$  octahedron in the lower layer. The two vertices of  $\alpha$ ,  $\beta$ , and  $\gamma$  are  $(\text{Ca}^{2+}, \text{Ca}^{2+})$ ,  $(\text{Sr}^{2+}, \text{Ca}^{2+})$ , and  $(\text{Ca}^{2+}, \text{Bi}^{3+})$ , respectively. Under the nearest neighbor interaction approximation, because  $\alpha$  and  $\beta$  maintain the symmetry of charges in the direction of the  $c$ -axis, the electrons in the octahedrons are strictly confined to the equilibrium position and become unmovable insulated electrons. Moreover, since the radius of  $\text{Ca}^{2+}$  (99 pm) is smaller than that of  $\text{Sr}^{2+}$  (113 pm), thus  $h_\alpha < h_\beta$ . In the case of  $\gamma$ , due to the charge asymmetry in the direction of the  $c$ -axis, the upward displacement of electrons leads to the stretching of  $h_\gamma$  and the symmetry breaking of the octahedron, which in turn reduces the restriction of  $\text{CuO}_2$  on electrons, making them displaceable conductive and superconducting electrons.

In our theoretical framework, the distance  $h$  between two vertices of the octahedron is a critical parameter, which not only determines whether the material can be superconducting and its superconducting transition temperature but also affects the structure of the Fermi surface. Based on experimental data and the qualitative analysis mentioned above, the  $h$  values of the three types of octahedrons in the Bi2223 superconductor

satisfy the following relationship:  $h_\alpha < h_\beta < h_\gamma$ , which implies that the binding energies  $E_B$  of the  $\Gamma$ -electrons in the ground state satisfy the inequality:  $E_B^\alpha > E_B^\beta > E_B^\gamma$ . In the previous section, it was indicated that the excited  $p$ -electrons contribute to the Fermi surface, and only when the  $p$ -electrons enter the corresponding four pockets in Fig. 2b can they be recorded by ARPES through the photoemission effect. In Bi2223 superconductors, the electrons within the  $\gamma$  octahedron with the smallest  $E_B^\gamma$  are the easiest to be detected by ARPES. Hence, as shown in Fig. 4b, the Fermi surface usually consists of a single green Fermi arc with a small energy gap  $\Delta_\gamma$ . In the case of overdoped samples, the lattice will be distorted, reducing the binding energy ( $E_B^\alpha$  and  $E_B^\beta$ ) between the confined electrons and the octahedrons. Hence, electrons from  $\alpha$  and  $\beta$  octahedrons may also be excited into the corresponding four Fermi pockets and captured as photoelectrons by ARPES, as indicated the red and blue Fermi arcs with energy gaps  $\Delta_\alpha$  and  $\Delta_\beta$  in Fig. 4b, respectively. Therefore, it is possible to observe one ( $\gamma$ ), two ( $\gamma, \beta$ ), or even three ( $\gamma, \beta, \alpha$ ) Fermi surface sheets in the ARPES experiment of the Bi2223 superconductor, as reported.

The second unusual behavior is why the maximum  $T_c$  of Bi2223 can persist in the overdoped region. This problem is relatively easy to explain qualitatively by using the new mechanism. Firstly, the middle  $\text{CuO}_2$  plane (MP) formed by  $\alpha$  octahedra is an insulating layer, and doping does not change its insulation characteristics. However, the  $\text{CuO}_2$  upper plane (UP) and lower plane (LP) isolated by the MP can independently exhibit superconductivity upon doping. Consequently, the three-layer structure of Bi2223 can be regarded as a dual superconductor. Initially, doping occurs solely in the LP, and when the doping reaches the optimal level ( $p \simeq 0.16$ ), the critical temperature  $T_c$  attains its maximum value in LP. As doping continues, the UP assimilates the excess carriers and enters a superconducting state. Meanwhile, the LP maintains its optimal doping state before the UP achieves its optimal level. As a result, the maximum value of  $T_c$  remains unchanged. Subsequently, when the UP reaches the optimal doping, corresponding to a total doping concentration of 0.32, further doping at this stage leads to the simultaneous entry of excess carriers into both the LP and UP. Consequently, the optimal superconducting state is disrupted, and the superconducting transition temperature declines.

### III. FE-BASED SUPERCONDUCTORS

As the second class of HTS, iron-based superconductors have a lower critical temperature than copper-based superconductors. However, their extensive family of compounds provides a much wider variety of experimental samples and data for studying high-temperature superconductivity mechanisms. Understanding the similarities and differences between these two classes of superconductors is essential for developing a comprehensive theory of high-temperature superconductivity.

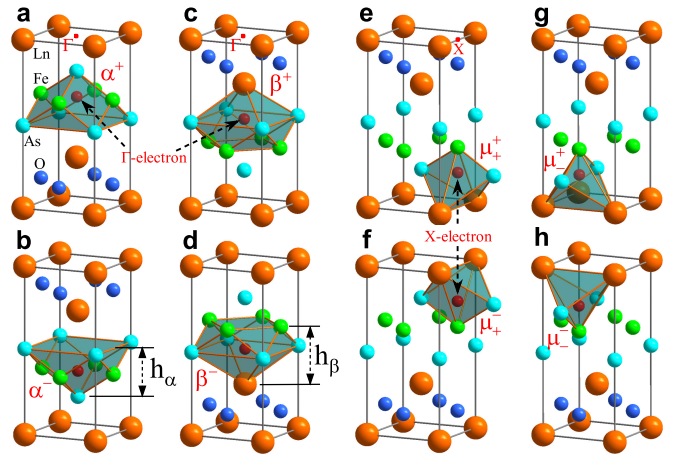


FIG. 5. Confined electrons in the iron-based 1111 superconductor. a and b The nonahedron confinement cages (quantum-well); c and d the tri-decahedron confinement cages; e - h the tetrahedron confinement cages.

#### A. Quantum confinement and $T_c$

The discovery of iron-based superconductors has generated significant interest in the scientific community due to their unique properties<sup>98</sup>. The 1111 series represents the first family of iron-based superconductors discovered and currently boasts the highest superconducting transition temperatures. This series can be denoted as  $\text{LnFeAsO}$ , where Ln represents elements including La, Sm, Ce, Nd, Gd, and F commonly substitutes the O position. The FeAs layer is a crucial structural component in iron-based superconductors, and the superconducting behavior is closely associated with these FeAs layers. Copper-based superconductors exhibit a two-dimensional  $\text{CuO}_2$  layer structure, whereas iron-based superconductors possess a folded layer structure of As-Fe-As. This structural disparity influences the electronic behavior and properties of these superconductors. Copper-based superconductors exhibit an anisotropic d-wave symmetry in their superconducting energy gap. In contrast, iron-based superconductors display more complex energy gap symmetries, including s-wave, d-wave, and  $(s\pm)$ -wave<sup>99-101</sup>, depending on the specific material and its doping level<sup>69,70</sup>.

Unlike the 2D  $\text{CuO}_2$  superconducting planes in copper-based superconductors, the FeAs layer has a sandwich structure of the As-Fe-As trilayer. According to the electron confinement mechanism proposed in this article, the electron confinement effect of FeAs is undoubtedly weaker than that of the  $\text{CuO}_2$  layer. Qualitatively, it can be predicted that the  $T_c$  of iron-based superconductors would be lower than copper-based superconductors.

Figure 5 shows the eight localized electronic states of three possible types in the 1111 superconductor. Figs. 5a and b are the  $\alpha^\pm$  phase of the nonahedron, Figs. 5c and d are the  $\beta^\pm$  phase of the tri-decahedron, and Figs. 5e-h are the  $\mu_\pm^\pm$  phase of the tetrahedron. The  $\alpha^\pm$  and  $\beta^\pm$  phases correspond to two pairs of degenerate states, where the electrons are localized respectively in the center of iron and arsenic layer cells; these

TABLE II. The relationship between  $T_c$  of iron-based superconductors and the height  $h$  of polyhedral quantum well,  $h = h_\alpha$  (or  $h_\beta, h_\gamma$ ), where  $\lambda_{Fe} = T_c h^2$ . The values in bold are possible superconducting phases.

Compound	$T_c$ (K)	$h_\alpha$ (Å)	$h_\beta$ (Å)	$h_\gamma$ (Å)	$\lambda_{Fe}$
$LaFeAsO_{1-x}F_x$	43	2.6723	<b>3.0749</b>		406
$SmFeAsO_{1-x}F_x$	43	2.7291	<b>3.0792</b>		407
$SmFeAsO_{1-x}F_x$	55	<b>2.7149</b>	3.0433		405
$TbFeAsO_{1-x}F_x$	45	2.7567	<b>3.0501</b>		418
$GdFeAsO_{1-x}F_x$	53.5	<b>2.7454</b>	3.0568		403
$PrFeAsO_{1-x}F_x$	52	<b>2.6857</b>	3.0591		375
$NdFeAsO_{1-x}F_x$	50	<b>2.7227</b>	3.0418		371
$CeFeAsO_{1-x}F_x$	41	2.6930	<b>3.0777</b>		388
$LaFeAsO$	41	2.6608	<b>3.0912</b>		392
$LaYFeAsO$	42	2.6840	<b>3.0912</b>		401
$BaKFe_2As_2$	38	2.7650	<b>3.3242</b>		419
$CaKFe_4As_4$	35	2.5617	2.9276	<b>3.3874</b>	402
$KCa_2Fe_4As_4F_2$	33	2.8406	3.0301	<b>3.4353</b>	390

four kinds of electrons contribute to the superconductivity. Each polyhedron represents a superconducting phase, and the height of the polyhedron determines the superconducting gap and the superconducting transition temperature. Since  $h_\alpha$  is smaller than  $h_\beta$ , the  $\alpha^\pm$  phase has a higher  $T_c$  than the  $\beta^\pm$  phase. In the case of the tetrahedron, the  $\mu_\pm^\pm$  phase restricts the  $X$ -electrons, which do not determine the superconducting gap or transition temperature. The restriction on electrons of  $\mu_\pm^\pm$  is the weakest, resulting in the most minor binding energy between the electron and the tetrahedron and corresponding to the smallest Fermi surface structure.

Similar to copper-based superconductors of Table I, some studies have identified a systematic correlation between the position of Fe ions and the superconducting critical temperature  $T_c$  through statistical means<sup>102,103</sup>. Table II shows the relationship between the superconducting transition temperature and the height of the  $\Gamma$ -electron polyhedra in iron-based superconductors. It can be observed that the majority of iron-based superconductors exhibit a dual-phase behavior, while a few can exhibit a triple-phase behavior. These findings can be verified through neutron spin resonance and pressure experiments, which will be discussed in detail later in the paper. Similarly, the relationship between the superconducting gap  $\Delta$ ,  $T_c$ , and  $h = h_{\alpha(\beta,\gamma)}$  can be obtained as

$$\Delta \propto T_c = \frac{\bar{\lambda}_{Fe}}{h^2} \simeq \frac{400}{h^2}. \quad (2)$$

The value  $\bar{\lambda}$  determines the strength of the restriction on superconducting  $\Gamma$ -electrons in superconducting materials. A larger  $\bar{\lambda}$  implies stronger electron localization and a higher  $T_c$ . Comparing Eq. (1) and Eq. (2), the value of  $\bar{\lambda}_{Cu} = 1320$  for copper-based superconductors is approximately three times that of  $\bar{\lambda}_{Fe} = 400$  for iron-based superconductors. It is known that copper-based superconductors achieved a record  $T_c$  of up to 164 K under high pressure<sup>104</sup>, while the record for iron-based superconductors is around 55 K<sup>9</sup>. It is

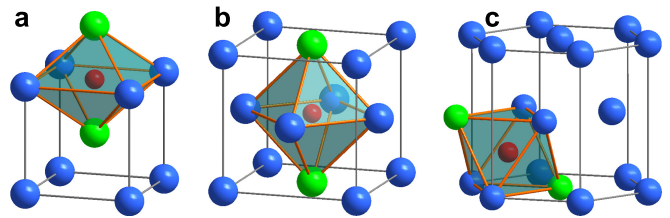


FIG. 6. The octahedral confinement of superconducting electrons in conventional elemental superconductors. a BCC, b CCP, and c HCP.

also surprising that the relationship between the two highest superconducting transition temperatures is just three times.

### B. D-wave, S-wave or S(+)-wave?

So far, whether it is copper-based or iron-based superconductors and whether it is theoretical or experimental research, the most critical question for superconductivity researchers is how electrons are paired. Because they firmly believe that the symmetry of the gap function is the key to unraveling the superconducting mechanism. This article presents an entirely different viewpoint on this matter. As shown in Fig. 2b, the so-called d-wave symmetry is merely the result of the localized electrons within the octahedron interacting with the nearest oxygen ions (negative charges) and the next-nearest copper ions (positive charges) in the  $CuO_2$  plane. In our opinion, the superconducting mechanism needs a new paradigm.

Generally, the energy gap in conventional superconductors is believed to possess typical s-wave symmetry. Figure 6 illustrates three typical crystal structures of elemental superconductors, whether it is body-centered cubic (BCC), face-centered cubic (CCP), or hexagonal close-packed (HCP). The octahedral cage can also describe confined superconducting electrons. Due to the crystal's symmetry, it is possible to construct six octahedra with different orientations around the same localized electron, implying that the confined superconducting electrons are isotropic and exhibit a six-fold degeneracy. Consequently, the symmetry of their superconducting energy gap can be approximated as an isotropic s-wave without the presence of nodes observed in quasi-2D copper-based superconductors.

The gap symmetry in iron-based superconductors has been a subject of debate. The most commonly observed gap symmetry in iron-based superconductors is an  $s\pm$ -wave symmetry. However, other gap symmetries, such as d-wave and s-wave, have also been proposed and reported. Fig. 7a shows the crystal structure of  $Ba_{1-x}K_xFe_2As_2$  (BKFA) from the 122 family with  $T_c = 38$  K, which has been extensively studied using ARPES due to its excellent crystal quality<sup>69</sup>.

The BKFA of Fig. 7a also exhibits two types of doubly degenerate superconducting electronic states, denoted as  $\alpha^\pm$  and  $\beta^\pm$ . The 38 K phase corresponds to the low- $T_c$   $\beta^\pm$  phase, while the high- $T_c$   $\alpha^\pm$  phase can be predicted with approximately 52 K based on the structural data in Table

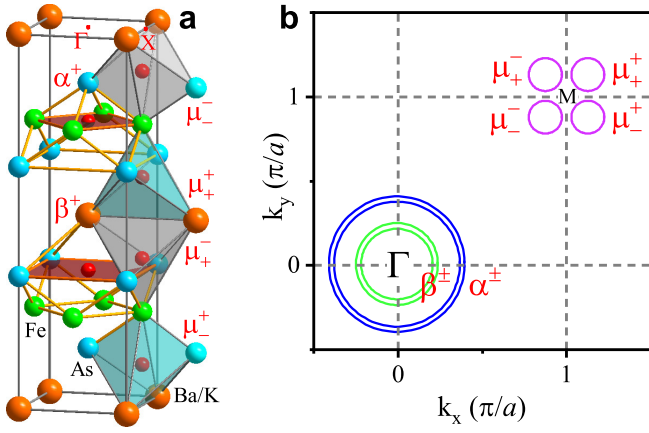


FIG. 7. Confined electrons and corresponding Fermi surfaces in an iron-based 122 superconductor. **a** Three kinds of eight localized electrons inside 122; **b** the corresponding eight Fermi surface.

II. The phase transition from the low- $T_c$   $\beta^\pm$  phase to the high- $T_c$   $\alpha^\pm$  phase is possible by pressure. This pressure-induced phase transition has already been achieved in similar superconductors like  $\text{KFe}_2\text{Se}_2$ <sup>105</sup>.

Regarding the size and symmetry of the energy gap, firstly,  $h_\alpha < h_\beta$ , then it can be concluded that the energy gap of the two superconducting phases satisfies:  $\Delta_\alpha > \Delta_\beta$ . As for the energy gap symmetry, it must be clear that it comes from the local symmetry of the polyhedral quantum well in Fig. 7a. Qualitatively, due to the absence of highly symmetric octahedra found in Fig. 6 of 3D elemental superconductors and the lack of octahedra containing strict 2D copper-oxygen planes like those in Fig. 2 for copper-based superconductors, therefore, the energy gap symmetry of iron-based superconductor is neither the s-wave of elemental superconductors nor the d-wave of copper-based superconductors, of course, due to the complexity of the inherent crystal structure's restricted polyhedra, it is not a strict  $S^\pm$ -wave. This issue does not require excessive attention and interpretation as it is not directly related to the superconducting mechanism.

The Fermi surface has always been imbued with a great deal of mystique, but in reality, it is just an image of the electron states in real space. In Fig. 7a, the eight electron states each contribute to a closed circular ring on the Fermi surface shown in Fig. 7b. The higher the binding energy between the localized electrons in real space and the polyhedral quantum well, the larger the corresponding radius of the Fermi surface. The  $\alpha^\pm$  and  $\beta^\pm$  electrons at the center point  $\Gamma$  of Fig. 7a contribute to two concentric large Fermi rings at  $\Gamma$  of Fig. 7b, while the four electrons at point  $X$  contribute to four small rings at point  $M(\pi, \pi)$  of Fig. 7b. As shown in Fig. 7b, the theoretical Fermi surface obtained based on the localized electrons in real space perfectly matches the experimentally reported results<sup>69,106</sup>.

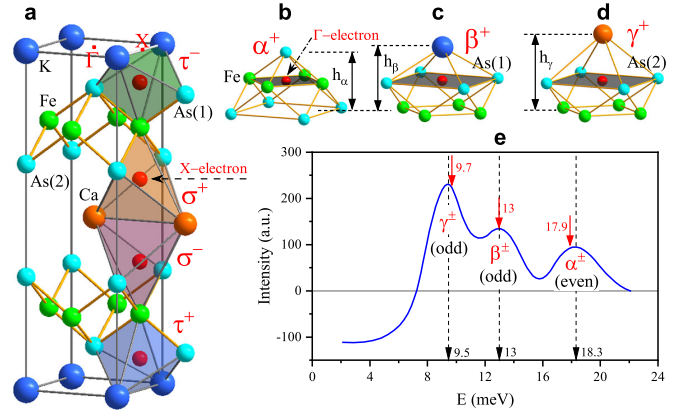


FIG. 8. Neutron spin resonance mode and mode symmetry of 1144 iron-based superconductors. **a** The crystal structure of  $\text{CaKFe}_4\text{As}_4$ , **b-d** three localized phases of  $\Gamma$ -electrons and corresponding confined polyhedrons, and **e** neutron spin resonance peaks and odd-even symmetry corresponding to three confined electrons.

### C. Resonant modes and symmetries in 1144 compound

The crystal structure of the 1144 iron-based superconductor closely resembles that of the 122 series. Research on the 1144 superconductors mainly focuses on  $\text{CaKFe}_4\text{As}_4$  of Fig. 8a. Comparing Fig. 8 and Fig. 7, two distinctions between the two compounds are apparent. Firstly, the 122 has two  $\Gamma$ -electron states ( $\alpha^\pm$  and  $\beta^\pm$ ), while the 1144 system has three  $\Gamma$ -electron states ( $\alpha^\pm$ ,  $\beta^\pm$  and  $\gamma^\pm$ ). This results in observing three double-degenerate Fermi surfaces in high-resolution laser-ARPES experiments on the 1144 series. Secondly, the 122 series has a quadruple degenerate  $X$ -electron. In comparison, the 1144 series has two doubly degenerate  $X$ -electrons, which leads to their slightly different Fermi surface at point  $M$ . From the confined polyhedron structure and quantity, 1144 shows greater similarity with 12442 of  $\text{KCa}_2\text{Fe}_4\text{As}_4\text{F}_2$  superconductor, leading to almost the same Fermi surface structure<sup>107</sup>.

This section focuses on the experimental results of inelastic neutron scattering conducted by Xie et al. on  $\text{CaKFe}_4\text{As}_4$ <sup>108</sup>. We explain the origins of the observed triplet spin resonance modes and odd-even symmetries. Here, the resonance modes observed in the neutron scattering experiment are believed to arise from the contribution of  $\Gamma$ -electrons. In Fig. 8, it can be observed that  $\text{CaKFe}_4\text{As}_4$  possesses three types of  $\Gamma$ -electrons, which are the nonahedron  $\alpha^\pm$  electron of Fig. 8b, the tri-decahedron  $\beta^\pm$  electron of Fig. 8c and the tri-decahedron electron  $\gamma^\pm$  of Fig. 8d. Each type of electron contributes to one definite spin resonance mode; hence, triplet spin resonance modes exist in the experiment. The resonance energy is directly proportional to the superconducting energy gap, as per Eq. (2), which establishes a relationship between the resonance energy and the height of the polyhedron of Figs. 8b-d as follows:

$$E_R = \frac{\Theta}{h_i^2}, \quad i = \alpha, \beta, \gamma, \quad (3)$$

where  $\Theta$  is the undetermined coefficient.

According to the crystal structure data of Ref.<sup>108</sup>,  $c = 12.63$  Å and  $zc = 5.855$  Å (the distance between adjacent Fe-Fe planes), resulting in  $h_\alpha = 2.504$  Å,  $h_\beta = zc/2 = 2.928$  Å, and  $h_\gamma = (1-z)c/2 = 3.387$  Å. As shown in Fig. 8e, assuming the resonance peak  $E_R(\beta)$  of phase  $\beta^\pm$  is 13 meV, by applying Eq. (3) we can determine the resonance peaks of phase  $\alpha^\pm$  and phase  $\gamma^\pm$  as  $E_R(\alpha) = 17.9$  meV and  $E_R(\gamma) = 9.7$  meV, which are consistent with the experimental values of 18.3 meV and 9.5 meV, respectively. In their experiments<sup>108</sup>, they observed that the spin resonance mode of the 1144 superconductor exhibits two modulation modes: odd mode and even mode. We believe this difference also comes from the nature of polyhedron. It can be seen from Fig. 8 that the  $\alpha^\pm$  electrons are confined in the Fe layer, corresponding to even symmetry, while  $\beta^\pm$  and  $\gamma^\pm$  electrons are confined in the As(1) and As(2) layers, respectively, corresponding to odd symmetry. The polyhedron structure determines this odd-even modulation of the spin resonance mode and cannot be used as evidence of superconducting pairing.

#### D. Fermi surface of single-layer FeSe superconductor

Due to their remarkable properties and potential applications, single-layer iron-based superconductors have garnered considerable interest. These materials comprise a solitary layer of iron atoms nestled between two layers of chalcogenide atoms. One particularly intriguing aspect of single-layer FeSe is its distinct Fermi surface, setting it apart from other iron-based superconductors (refer to Fig. 7b). The Fermi surface of FeSe consists of pockets near the zone corner, devoid of any indication of a Fermi surface around the zone center<sup>67</sup>. The underlying reason for this distinctive Fermi surface structure remains a mystery.

In the single-layer FeSe superconductor, only the local electronic state of phase  $\alpha^+$  in Fig. 9a exists, and the electrons are entirely confined in the central Fe layer. According to Table II, the highest superconducting transition temperature of iron-based superconductor  $\alpha^+$  phase is about 55 K, which is entirely consistent with the conclusion by analyzing the temperature dependence of the superconducting gap<sup>67</sup>. Fig. 9b depicts a top view of a single-layer FeSe superconductor with localized electrons, while Fig. 9c shows the corresponding Fermi surface. Because there are no localized electrons at point  $\Gamma$  in Fig. 9b, it is observed that the central area of the Fermi surface in Fig. 9c does not exist, but the Fermi surface appears at four corners.

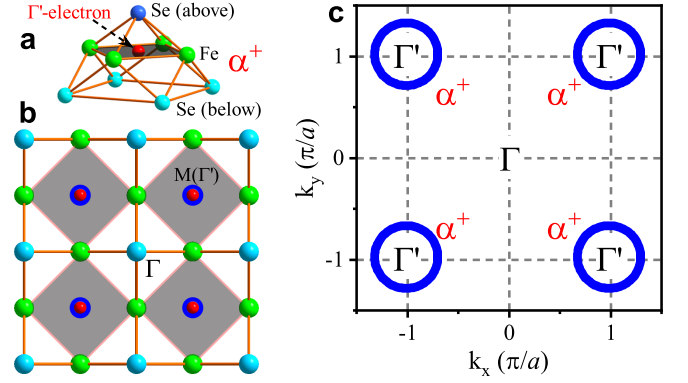


FIG. 9. The Fermi surface mapping of monolayer FeSe superconductor. **a** Localized electrons confined by the nonahedron quantum well, **b** the top view structure of FeSe superconductor, **c** the Fermi surface corresponding to **b**.

#### E. Pressure-induced superconducting phase transition

Pressure significantly influences the behavior of superconductors by inducing structural changes that can modify their electronic properties and impact superconductivity. In 2012, Sun et al. studied the effect of pressure on iron-based superconductors, particularly  $K_{0.8}Fe_ySe_2$ <sup>105</sup>. Surprisingly, they observed a second phase transition in superconductivity triggered by pressure. This discovery revealed the coexistence of two distinct superconducting phases within the same material, each characterized by different transition temperatures. This finding challenges existing theories on superconductivity, suggesting the need for a new framework to explain the presence of multiple superconducting phases and their respective transition temperatures. The discovery emphasizes the importance of further exploration and a deeper understanding of superconductivity, which may pave the way for developing innovative superconducting theories.

Next, we will show that the mechanism of pressure-increasing superconducting transition temperature can be well understood within the framework of confined electrons. In this paper, Eq. (2) provides insights into the direct influence of pressure on the height of polyhedral quantum wells in iron-based superconductors. With the application of pressure, the height of the quantum well decreases, which leads to a decrease in the mobility of confined electrons. This reduced mobility can enhance the localization of electrons, potentially leading to a higher  $T_c$  superconducting phase.

As shown in Figs. 10a and b, in  $K_{0.8}Fe_ySe_2$  superconductors, two types of polyhedron quantum wells can be constructed, each confining localized electrons of type  $\alpha^\pm$  and  $\beta^\pm$ , respectively. These electrons correspond to different superconducting phases: the low-temperature  $\beta^\pm$  phase, or the first superconducting phase, represented by Fig. 10a, and the high-temperature  $\alpha^\pm$  phase, or the second superconducting phase, represented by Fig. 10b. With known values of  $h_\alpha = 2.836$  Å and  $h_\beta = 3.534$  Å, according to Eq. (2), the highest superconducting transition temperatures for

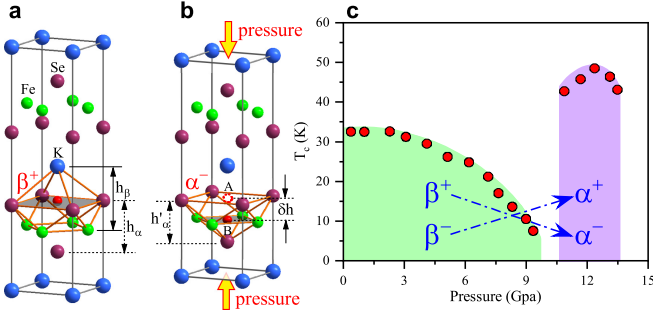


FIG. 10. Illustrate the pressure-induced phase transition of intrinsic double superconducting phases in  $K_{0.8}Fe_ySe_2$  superconductor. **a** The low- $T_c$  superconducting  $\beta$  phase without external pressure; **b** the localized electron transfer from A of Se-plane ( $\beta^+$  phase) to B of Fe-plane and the emergence of high- $T_c$   $\alpha$  phase due to pressure; **c** the phase diagram illustrating the phase transition process.

the respective phases can be accurately predicted as 32.1 K for  $\beta^\pm$  phase and 49 K for  $\alpha^\pm$  phase. These two values closely match the experimentally observed highest transition temperatures, 32K and 48.7 K, for the first and second superconducting phases<sup>105</sup>.

In fact, the microscopic electronic behavior of this phase transition process is very simple. In the absence of external pressure, the initial state of electrons in  $K_{0.8}Fe_ySe_2$  corresponds to the low-temperature superconducting phase  $\beta^\pm$  with a transition temperature of approximately 32 K, where the electrons are localized in the Se layer. Under external pressure, the lattice undergoes slight distortion, causing the electrons to transfer from the Se layer to the Fe layer, as illustrated in Fig. 10b, with a shift in position  $\delta h$  of approximately 1.4 Å from A to B. As shown in Fig. 10c, in this process, a phase transition of the superconducting phase occurs ( $\beta^+ \rightarrow \alpha^-$ ,  $\beta^- \rightarrow \alpha^+$ ), where the low-temperature phase  $\beta^\pm$  above 32 K disappears, and the high-temperature phase  $\alpha^\pm$  above 49 K emerges.

From the above sections, we show that many vital experiments of copper-based and iron-based superconductors can be well explained only by using the hypothesis of static localized electrons, which is enough to prove that the traditional superconducting theoretical research based on dynamic free electrons is flawed.

#### IV. UNIFIED SUPERCONDUCTING MECHANISM

Through the above research on copper-based and iron-based superconductor experiments, it is easy to see that superconductivity can be perfectly analyzed in a static localized electron framework, and the physical phase transition can be realized only by a slight displacement of electrons of angstrom level. Based on the above research, we propose a unified microscopic mechanism based on Mott insulators with localized electrons, where current and magnetic fields are attributed to Maxwell displacement current and Dirac magnetic monopoles rather than electron

motion. Our proposal traces natural magnetic phenomena to the simplest electron-proton pair, where the pairing generates a magnetic field and individual electrons or protons generate an electric field. The proton-electron electric dipole vector is the Ginzburg-Landau order parameter for the superconducting phase transition<sup>81</sup>.

#### A. What are magnetic monopoles?

The duality between electric and magnetic fields is a fundamental concept in electromagnetism, which implies that generating a magnetic field requires static magnetic charges, as Dirac proposed in the theory of magnetic monopoles. It was suggested that electric and magnetic charges could coexist and satisfy the following quantization condition<sup>80</sup>:

$$eg = \frac{hc}{4\pi}n = \frac{\hbar c}{2}n, \quad n = \pm 1, \pm 2, \pm 3, \dots \quad (4)$$

where  $e$  and  $g$  are the electric and magnetic charges, respectively,  $h$  is the Plank's constant, and  $n$  being the integers.

Using the fine structure constant  $\alpha = e^2/4\pi\epsilon_0\hbar c$ , the Eq. (4) can be re-expressed as:

$$g = \left(\frac{n}{8\pi\epsilon_0\alpha}\right)e = \Pi_n e, \quad n = \pm 1, \pm 2, \pm 3, \dots \quad (5)$$

where  $\Pi_n$  is an adjustable constant.

The relationship presented in Eq. (5) above provides a clear understanding that the purported magnetic monopoles are, in fact, just dressed electrons or protons. This means that the superimposed electric field created by the electron-proton pair is the magnetic field. Intriguingly, electrons and protons can simultaneously act as electric and magnetic charges. In the

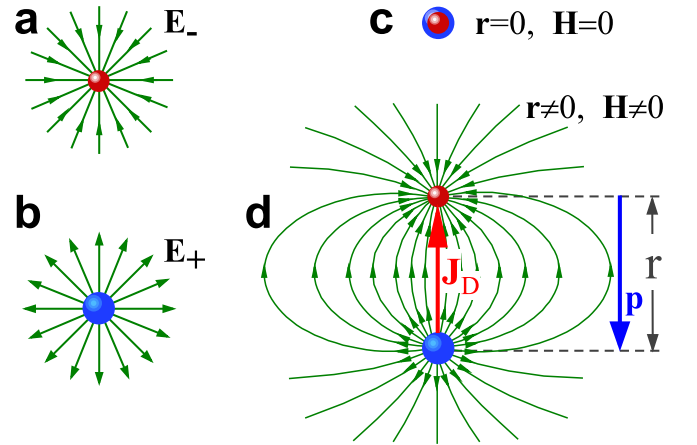


FIG. 11. Relationship between electrostatic field and static magnetic field. **a** and **b** Isolated charges produce electric fields; **c** due to the symmetry ( $r = 0$ ), the magnetic field is hidden; **d** when the symmetry is broken ( $r \neq 0$ ), the magnetic field emerges.

following, we will reconfirm this conclusion in accordance with Maxwell's theory.

Figs. 11a and b show isolated electron or proton generating electric fields  $\mathbf{E}_-$  and  $\mathbf{E}_+$  respectively. As in Fig. 11c, no electromagnetic field exists when coinciding. In Fig. 11d, a separation of  $\mathbf{r}$  forms an electric dipole through symmetry breaking, and a magnetic field emerges. It is well-known that a proton-electron pair can form a hydrogen atom or a neutron, and it is worth emphasizing that the proton-electron pair is the smallest quantized capacitance in nature. According to Maxwell's theory, a displacement current density  $\mathbf{J}_D = \varepsilon_0 \partial \mathbf{E} / \partial t$  exists in the capacitor, which will create an associated magnetic field in the surrounding space. As Maxwell's statement suggests, a changing electric field produces a magnetic field, which is given by  $\mathbf{H}$  as follows:

$$\mathbf{B} = \mu_0 \mathbf{H} = \frac{\mathbf{E}_+ + \mathbf{E}_-}{c}, \quad (6)$$

where  $c$  is the speed of light and  $\mu_0$  is the vacuum permeability.

### B. Symmetry of Maxwell's equations

Maxwell's equations are elegant but not invariant under duality transformation. Is the asymmetry between electric and magnetic fields a reflection of nature or our interpretation? We will provide a clear answer. The Maxwell's first equation  $\nabla \cdot \mathbf{E} = \rho_e / \varepsilon_0$  and the second equation  $\nabla \cdot \mathbf{B} = 0$  are completely independent of each other, so strictly speaking, the electromagnetic field is not unified. Here, we will show that the second equation can be derived from the first. For a proton-electron pair with an electric dipole vector of  $\mathbf{p}$ , substituting the electric fields excited by the electron and proton into Eq. (6) yields:

$$\nabla \cdot \mathbf{B} = \frac{[\rho_e(\mathbf{r}_p) + \rho_{-e}(\mathbf{r}_p + \mathbf{p}/e)]}{c\varepsilon_0}. \quad (7)$$

Under a far-field approximation  $\mathbf{r}_p \gg \mathbf{p}/e$ , then  $\rho_e(\mathbf{r}_p) + \rho_{-e}(\mathbf{r}_p + \mathbf{p}/e) \simeq 0$ , this result means that the right-hand side of the second Maxwell's equation is not exactly zero. Furthermore, our assumption has ruled out the presence of the conduction current ( $\mathbf{J}_e = 0$ ). Thus far, we can now present the corrected Maxwell's equations:

$$\begin{aligned} \nabla \cdot \mathbf{E} &= \frac{\rho_e}{\varepsilon_0}, \\ \nabla \cdot \mathbf{B} &\simeq 0, \\ \nabla \times \mathbf{E} &= -\frac{\partial \mathbf{B}}{\partial t}, \\ \nabla \times \mathbf{B} &= \mu_0 \varepsilon_0 \frac{\partial \mathbf{E}}{\partial t}. \end{aligned} \quad (8)$$

Eq. (8) has two breakthroughs: (1) the new first and second equations are linked, describing electric and magnetic

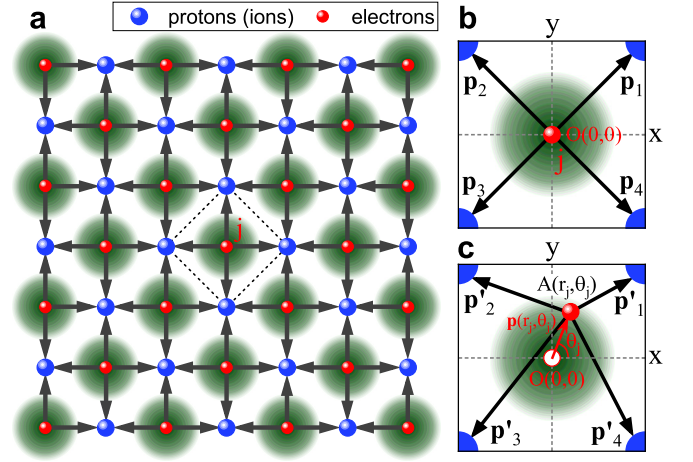


FIG. 12. a The electric dipole vector represents 2D Mott insulator with the intrinsic antiferromagnetic long-range order, b a localized electron in ground state; c the electron in excited state.

fields respectively, and (2) the absence of conduction current leads to symmetry in the third and fourth equations. Based on the first and second of Eq. (8), a crystal composed of electron-proton (ion) pairs can be viewed as a super large-scale integrated capacitor. The current is interpreted as an electromagnetic wave with the third and fourth equations. As a result, research on avoiding collisions between electrons and the lattice in superconductivity has been transformed into an investigation into reducing the loss of electromagnetic waves during propagation within superconductors.

### C. Mott insulator and order parameters

The above research has shown that the energy gap symmetry is not the key to superconductivity, but the key to the superconductivity mechanism is the localization of electrons. For the convenience of discussion, we ignore the influence of negatively charged ions on the energy gap symmetry around the localized electrons. In that case, both conventional and unconventional superconductors can be simplified to the quasi-two-dimensional Mott crystal structure in Fig. 12a, and the green contour line represents the Coulomb field of the ions in the nearest adjacent layers. Under this assumption, we can establish a unified superconducting theory suitable superconductors. When Fig. 12a is decorated with the electric dipole vectors, showing the inherent antiferromagnetic long-range order. If capacitors represent the electron-proton pairs, the total capacitance of the Mott insulator is zero due to symmetry. Therefore, it appears as an insulator that cannot conduct electricity.

Fig. 12b is the unit cell, where four degenerate electric dipole vectors ( $\mathbf{p}_1, \mathbf{p}_2, \mathbf{p}_3,$  and  $\mathbf{p}_4$ ) can be integrated into a total vector  $\mathbf{P}_0 = 0$ . As shown in Fig. 12c, external factors (temperature, pressure, and electromagnetic fields) can cause the ground state electron to enter an excited state  $A(r_j, \theta_j)$  with a vector  $\mathbf{p}(r_j, \theta_j) = e\mathbf{r}_j$ . The sum of four electric

dipole vectors ( $\mathbf{p}'_1, \mathbf{p}'_2, \mathbf{p}'_3,$  and  $\mathbf{p}'_4$ ) is expressed as  $\mathbf{P}_A = -\mathbf{p}(r_j, \theta_j) = -er_j \exp(i\theta_j)$ . The emergence of the vector  $\mathbf{P}_A$  indicates the excitation of a hidden magnetic state in the superconducting parent, leading to the destruction of the Mott antiferromagnetic phase. Moreover, the vector can function as the spin and magnetic moment of the excited electrons. It is worth noting that the magnetism or spin of an electron arises from a combination of positively charged lattices. The electron loses its spin property upon departing from the material and becoming free, which can effectively explain the commonly observed charge-spin separation phenomenon in high-temperature superconducting materials.<sup>109</sup>

The Ginzburg-Landau theory is the most successful theory of superconductivity, capturing the order parameter and symmetry breaking of superconducting phase transition. However, it cannot address the microscopic question of what constitutes the order parameter with electromagnetic properties. Our theory can answer this question. For a conductor with  $N$  valence electrons, by using  $\mathbf{P}_A$ , the complex order parameter can be defined as:

$$\mathbf{P}_{order} = \frac{e}{N} \sum_{j=1}^N r_j \exp(i\theta_j). \quad (9)$$

Next, we will use Eq. (9) to distinguish among typical condensed states and display their essential differences at the microscopic scale.

## V. ZERO RESISTANCE AND MEISSNER EFFECT

The zero electrical resistance exhibited by superconductors in the presence of an applied electric field and the manifestation of the Meissner effect in the presence of a magnetic field are two crucial criteria for determining superconductivity. However, at the microscopic level, the changes in superconducting electrons inside the material before and after the phase transition still need to be fully understood. This lack of understanding is why research in superconductivity theory has become stuck. In the following, we aim to unveil the microscopic origins of these two key superconducting phenomena.

### A. The Essence of Zero Resistance in Superconductivity

In order to interpret the cause of zero resistance more intuitively, Fig. 12a can be further simplified as the superconducting surface of Fig. 13a. Under the condition of no external electromagnetic field and  $T < T_c$ , as shown in the projection Fig. 13b along  $X$  and  $yz$  direction, all electrons are in the ground state without symmetry breaking. At this time, the order parameter  $\mathbf{P}_{order}$  and the total capacitance of the superconductor are all zero, and the superconductor behaves as an antiferromagnetic insulator. Therefore, as a necessary condition, the ground state of any superconductor must be a Mott insulator. For good conductors like Au,

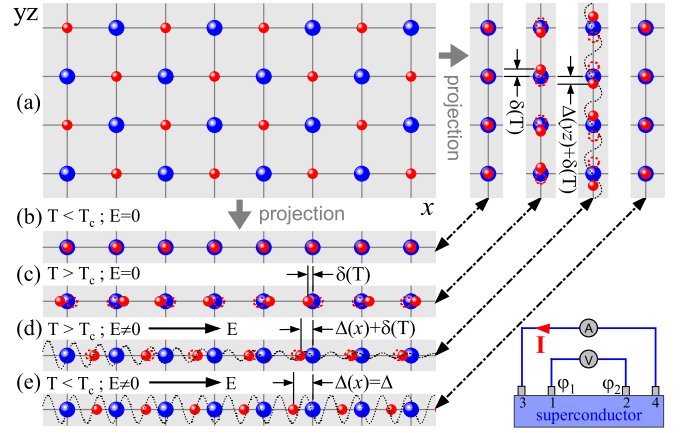


FIG. 13. Four condensed states based on symmetry and symmetry breaking. **a** Insulating state; **b** the projection of **a** along  $x$  and  $yz$  direction exhibits a perfect symmetry; **c** normal state under random thermal motion; **d** when  $T > T_c$ , metallic state driven by the electric field; **e** when  $T < T_c$ , the superconductor entering a completely symmetrical broken superconducting state, where all electrons have the same displacement in the opposite direction of the electric field. The insulating state (**a**) is the preparatory state for the superconducting state (**e**). Good conductors like gold, silver, and copper are not superconductors because existing low-temperature techniques cannot first bring them into the preparatory insulating state of **a**.

Ag, and Cu, because valence electrons are very active, they cannot condense into the insulating state at the lowest temperature that can be realized in the lab, so they do not exhibit superconductivity. When measuring Fig. 13a or Fig. 13b using the four-wire method, the potentials ( $\varphi_1$ ) and ( $\varphi_2$ ) on the superconducting surface induced by voltage electrodes 1 and 2 are both zero due to the cancellation of potentials generated by positive and negative charges inside the superconductor.

The second scenario depicted in Fig. 13c is the normal state, when  $T > T_c$ , the electrons absorb random thermal energy and then leave their equilibrium position with random displacement  $\delta(T)$  both in  $x$  and  $yz$  directions. Since random thermal motion does not destroy the overall symmetry, the superconductors' average order parameters  $\mathbf{P}_{order}$  and total capacitance remain zero.

Fig. 13d represents the metallic state. Assuming an external electric field is applied along the  $x$ -direction, when  $T > T_c$ , due to the combined effect of electric field and random thermal motion, electrons undergo displacements  $\Delta(x) + \delta(T)$  and  $\Delta(yz) + \delta(T)$  in the directions parallel and perpendicular to the electric field, normally,  $|\Delta(x)| \gg |\Delta(yz)|$ . As a result of thermal motion, the electromagnetic field energy does not propagate strictly along the  $x$ -direction but experiences losses along the  $yz$ -direction. In other words, as the propagation distance  $x$  increases, the electromagnetic field energy (or current) gradually attenuates, and the attenuated electromagnetic energy is manifested as losses in the  $zy$ -direction, contributing to the resistance. In this scenario, the potentials  $\varphi_1 > \varphi_2 \neq 0$ , resulting in a voltage

between the two electrodes,  $V = \varphi_1 - \varphi_2 \neq 0$  and the resistance  $R = V/I \neq 0$ .

Fig. 13e illustrates the superconducting state in which thermal disturbance is wholly suppressed. This state arises from a Pierce-like dimerization pairing transition that leads to perfect symmetry breaking along the direction of the applied electric field, while no symmetry breaking occurs in the vertical  $yz$ -direction. Since the electric field energy (current) does not decay, the displacement  $\Delta(x) = \Delta$  of the electrons is the same for all. As a result, the order parameter of Eq. (9) describing the superconducting phase transition reaches its maximum value  $\mathbf{P}_{order} = e\Delta$ . This means that all electrons undergo coherent condensation and enter the superconducting state. Because  $\Delta$  is a constant quantity, therefore  $\varphi_1 = \varphi_2 \neq 0$  and  $V = \varphi_1 - \varphi_2 = 0$ ; consequently, the resistance  $R = V/I$  becomes zero, indicating zero resistance in the experiments.

In the new paradigm as shown in Fig. 13, the essence of electric current is the energy of the input electromagnetic field. The main difference between the metallic and superconducting states lies in the presence or absence of energy loss during the transmission of electromagnetic energy. In the case of the superconducting state, electrons undergo a symmetric breaking only along the electric field direction, forming some array of capacitors, which opens up a lossless pathway for the propagation of electromagnetic energy. On the other hand, in the metallic state, the capacitive path perpendicular to the electric field is also opened, leading to the leakage of electromagnetic field energy and the formation of resistance. Suppose the valence electrons are severely bound and cannot undergo a symmetrical breaking phase change under the influence of an external field. In that case, the capacitor path will remain closed, and the material will stay in a non-conductive insulation state. Because electrons are no longer the carriers of electric energy, the transmission of current does not need the long-distance movement of electrons in the lattice. The problem of avoiding the collision between moving electrons and lattice in superconducting research, which has long plagued the physics community, does not exist.

## B. Meissner effect puzzle

Besides exhibiting zero resistivity, superconductors are also characterized by impeccable diamagnetism, referred to as the Meissner effect. As illustrated in Fig. 14, it is generally believed that when a superconductor is placed in a weak external magnetic field  $\mathbf{H}$ , the magnetic field is expelled from the interior if it cooled below its transition temperature. The magnetic field expelled picture of Fig. 14 shows that the Meissner effect is a time-dependent dynamic process. Hence, a correct theory of superconductivity must have the physics to explain how the superconductor goes from the normal to the superconducting state by expelling the magnetic field against Faraday's law. Since the experiment in 1933, many theories and mechanisms have been proposed to explain the Meissner effect. As Hirsch argued<sup>110</sup>, these mechanisms have not

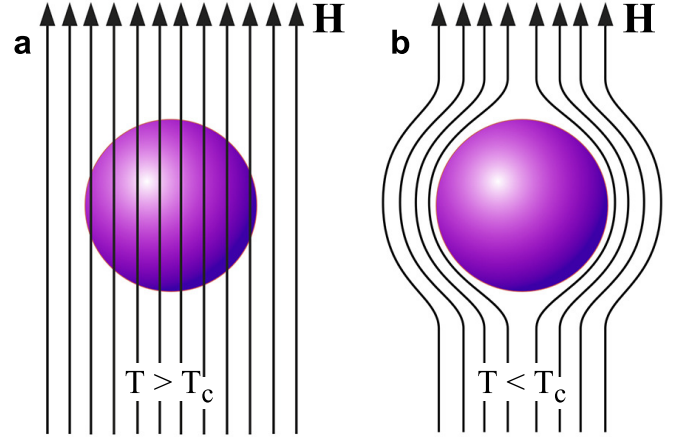


FIG. 14. Schematic diagram of Meissner effect. **a** Above the critical temperature, the magnetic field is able to penetrate the superconductor, **b** below the critical temperature, the magnetic field is excluded from the interior of the superconductor.

consistently described the Meissner experiment. In this study, we will solve this puzzle using the microscopic mechanism of proton-electron electric dipole pairing.

Before starting the following investigation, it is vital to look at the experiment of the Meissner effect<sup>111</sup>. Figure 15 shows two screenshots of the experiment, clearly showing that the superconductor and the magnet can both repel as demonstrated in Fig. 15a or attract as demonstrated in Fig. 15b each other. Moreover, repulsion and attraction can be switched instantaneously. One can immediately find that the magnetic field expulsion mechanism of Fig. 14b cannot explain the experimental fact that the superconductor and magnet of Fig. 15b are attracted to each other. To better explain the Meissner effect, we make a force analysis on the magnetic suspension in Fig. 15a and the superconductor suspension in Fig. 15b, respectively. Assuming the masses of the magnet and superconductor are  $m$  and  $M$ , respectively, the repulsive and attractive forces satisfy the force balance:

$$F_R = mg; \quad F_A = Mg, \quad (10)$$

where  $g$  is the acceleration of gravity.

The Eq. (10) seems simple but contains important information about the Meissner effect. First, the direction of the Meissner effect is automatically adjustable, which can make the magnet and the superconductor attract or repel each other. Second, according to the formula, the Meissner effect can also automatically modulate its strength to balance gravity according to the mass of the magnet or superconductor. From a personal point of view, this experiment's result is the biggest challenge for theoretical superconductivity researchers.

According to our theoretical framework, in the absence of an external magnetic field and a temperature below the superconducting critical temperature, all valence electrons will rest at a position with zero potential energy as indicated by the white circle in Figs. 15c and d. When a magnet ( $\mathbf{H}_{ext}$ ) is placed over a superconductor, due to the gravitational

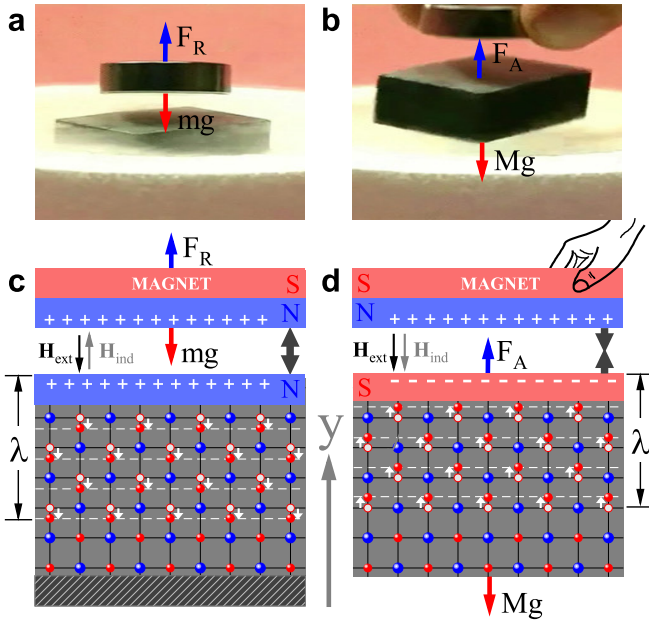


FIG. 15. The Meissner experiment and new explanation: **a** and **b** observed repulsion and attraction interactions; **c** and **d** corresponding theoretical explanations of confined electrons. In the figure,  $\lambda$  is the symmetrical breaking depth that can be automatically adjusted according to external factors.

field, the magnet tends to fall to increase the strength of the magnetic field within the superconductor. During this dynamic process, the electric field generated by the changing magnetic field directly leads to the downward displacement of electrons near the superconductor's surface and causes local symmetry breaking. As a result, it generates an induced magnetic field  $\mathbf{H}_{ind}$  in the opposite direction and a repulsive interaction between the magnet and the superconductor due to the same sign of charges on adjacent surfaces.

Fig. 15d shows that lifting the magnet away causes a decrease in magnetic field strength within the superconductor. Similar to the case of Fig. 15c, the electric field generated by the change of magnetic field forces the electrons near the superconducting surface to deviate from the equilibrium position upwards. Therefore, the induced magnetic field  $\mathbf{H}_{ind}$  in the same direction as  $\mathbf{H}_{ext}$ , leading to mutual attraction between the magnet and superconductor due to the net charge on their nearest neighboring surfaces being of different signs. In the figure,  $\lambda$  is the symmetry breaking depth, equivalent to the famous London penetration depth<sup>11,12</sup>. It must be pointed out that  $\lambda$  is not a fixed value, and it will be automatically adjusted according to external factors, such as the mass of magnets and superconductors, to achieve force balance.

From our explanation above, the nature of the Meissner effect is not mysterious. It is merely a simple magnetic interaction between a magnetized superconductor and a magnet. They follow the fundamental principle of “two identical poles repel, and two opposite poles attract”. Whether the magnet and the superconductor repel or attract can be automatically adjusted by the electrons deviating downward

or upward from the equilibrium position.

## VI. CONCLUDING REMARKS

In conclusion, we have established a theoretical framework centered around polyhedron quantum-well-confined electrons, building upon experimental evidence from STM, STS, ARPES and neutron scattering in high-temperature copper-based and iron-based superconductors. This research represents a groundbreaking and innovative approach, replacing the dynamic paradigm of free electrons with a static paradigm of localized electrons. By incorporating four well-established scientific hypotheses, namely the Mott insulator, Maxwell's displacement current, the Dirac magnetic monopole, and the Ginzburg-Landau symmetry-breaking theory, we have successfully developed a unified superconducting theory applicable to both conventional and unconventional superconductors.

This new theory merges electric and magnetic fields, revealing the intrinsic connection between magnetism and superconductivity while achieving the symmetry of Maxwell's equations. Within this unified theoretical framework, we have effectively explained numerous fundamental phenomena observed in high-temperature superconductors and condensed physical phase transitions. It enables the analytical determination of critical properties in copper-based and iron-based superconductors, for example, the structure of the Fermi surface, the value and symmetry of the superconducting energy gap, the superconducting transition temperature, and the spin resonance peak parity. Remarkably, the predictions of our theory align well with experimental findings. Moreover, our research offers fresh insights into the microscopic nature of the Ginzburg-Landau order parameter, the phenomenon of zero resistance, and the Meissner effect. We propose that the symmetry-breaking induced proton-electron pairing mechanism holds the potential to shed new light on various physical phenomena.

In the past few decades, it is undeniable that progress in the field of physics has stagnated, leading to a lack of consensus despite the numerous approaches taken to understand high-temperature cuprate superconductivity. Modern physics has often resembled the story of ‘blind men touching an elephant,’ especially in its early days when researchers, constrained by experimental limitations, heavily relied on subjective speculation. This reliance gave rise to numerous erroneous concepts and principles, which have been perpetuated and amplified by subsequent researchers. The extensive use of complex mathematical derivations and computers has further obscured fundamental errors and misdirected the trajectory of physics research.

Take the electron as an example; it has been burdened with many properties beyond its charge and mass, including spin, quantum entanglement, the Pauli exclusion principle, persistent currents, photon emission and absorption, and Cooper pairing. When pursuing concepts and modeling becomes fashionable, physics research inevitably veers down an irreversible path. However, it is important to

acknowledge that any motion in nature is not eternal, and the motion of electrons inherently involves energy loss. Even without considering the strong Coulomb interaction between lattice ions and electrons, the collective motion of a large number of electrons will inevitably exhibit diffusion and scattering. These are objective facts based on the laws of thermodynamics and electromagnetism. The assumption of a dynamic picture with randomly moving electrons cannot account for coherent condensation and superconductivity. In contrast, this paper suggests that simplifying the complexity and focusing on the static ground state of electrons with minimal energy allows for their coherent condensation, leading to the realization of superconductivity.

Through the research presented in this article, we hope the physics community can realize that physics can have a bright future only if it is based on experimental facts rather than subjective imagination. It should be emphasized that a candidate theory of superconductivity must first pass falsifiability tests in R-space. Instead of being obsessed with the virtual K-space, returning to the real space of matter is a

better choice. The reason is simple: R-space and K-space do not have a one-to-one correspondence, and a given physical system in R-space have infinitely many possible descriptions in K-space.

## ACKNOWLEDGMENTS

The author would like to acknowledge Prof. Duan Feng for his invaluable suggestions and helpful discussions at the early stage of this research. The author would also like to express his appreciation to Prof. Changde Gong for the opportunity to comprehend the fascinating world of superconductivity. Special thanks go to Prof. Dingyu Xing for his supportive and considerate care of the author's personal and family. Finally, the author extends his deepest gratitude to Prof. Shusheng Jiang for his unwavering encouragement, support of the research process, and provision of living arrangements and research resources.

\* xiuqing\_huang@163.com

- <sup>1</sup> Onnes, H. K. The Resistance of Pure Mercury at Helium Temperatures. *Leiden Comm.* **119b**, 122-130 (1911).
- <sup>2</sup> Bardeen, J., Cooper, L. N. & Schrieffer, J. R. Theory of Superconductivity. *Phys. Rev.* **106**, 162-164 (1957).
- <sup>3</sup> Bednorz, J. G. & Müller, K. A. Possible High- $T_c$  Superconductivity in the Ba-La-Cu-O System. *Z. Phys. B.* **64**, 189-193 (1986).
- <sup>4</sup> Wu, M. K. et al. Superconductivity at 93 K in a New Mixed-Phase Y-Ba-Cu-O Compound System at Ambient Pressure. *Phys. Rev. Lett.* **58**, 908-910 (1987).
- <sup>5</sup> Chu, C. W. et al. New High- $T_c$  Superconductor Y-Ba-Cu-O Compounds: Synthesis, Structure, Properties, and Phase Diagram. *Phys. Rev. Lett.* **58**, 405-407 (1987).
- <sup>6</sup> Maeda, H., Tanaka, Y., Fukutomi, M. & Asano, T. A New High- $T_c$  Oxide Superconductor Without a Rare Earth Element. *Jpn. J. Appl. Phys.* **27**, L209-210 (1988).
- <sup>7</sup> Kamihara, Y., Watanabe, T., Hirano, M. & Hosono, H. Iron-Based Layered Superconductor  $\text{La}[\text{O}_{1-x}\text{F}_x]\text{FeAs}$  ( $x = 0.05-0.12$ ) with  $T_c = 26$  K. *J. Am. Chem. Soc.* **130**, 3296-3297 (2008).
- <sup>8</sup> Chen, X. H. et al. Superconductivity at 43 K in  $\text{SmFeAsO}_{1-x}\text{F}_x$ . *Nature* **453**, 761-762 (2008).
- <sup>9</sup> Ren, Z. A. et al. Superconductivity at 55 K in Iron-Based F-Doped Layered Quaternary Compound  $\text{Sm}[\text{O}_{1-x}\text{F}_x]\text{FeAs}$ . *Chin. Phys. Lett.* **25**, 2215-2216 (2008).
- <sup>10</sup> Ren, Z. A., & Zhao, Z. X. Research and Prospects of Iron-Based Superconductors. *Adv. Mater.* **21**, 4584-4592 (2009).
- <sup>11</sup> Wen, H. H., Mu, G., Fang, L., Yang, H., & Zhu, X. Superconductivity at 25 K in hole-doped  $(\text{La}_{1-x}\text{Sr}_x)\text{OFeAs}$ . *EPL*, **82**, 17009 (2008).
- <sup>12</sup> Anderson, P. W. The Resonating Valence Bond State in  $\text{La}_2\text{CuO}_4$  and Superconductivity. *Science* **235**, 1196-1198 (1987).
- <sup>13</sup> Halboth, C. J. & Metzner, W. Nesting, Berry Phase, and Fermi-Liquid Behavior in Layered Metals. *Phys. Rev. Lett.* **85**, 5162-5165 (2000).
- <sup>14</sup> Baskaran, G. & Anderson, P. W. Gutzwiller's Renormalization Group Theory of the Hubbard Model: Implications for High- $T_c$  Superconductivity. *Phys. Rev. B* **37**, 580-584 (1988).
- <sup>15</sup> Zhang, F. C. & Rice, T. M. Effective Hamiltonian for the Superconducting Cu Oxides. *Phys. Rev. B* **37**, 3759-3761 (1988).
- <sup>16</sup> Lee, P. A. Amperean pairing and the pseudogap phase of cuprate superconductors. *Physical Review X* **4**, 031017 (2014).
- <sup>17</sup> Scalapino, D. J., Loh, Jr., E. & Hirsch, J. E. d-Wave Pairing Near a Spin-Density-Wave Instability. *Phys. Rev. B* **34**, 8190-8192 (1986).
- <sup>18</sup> Li, Z. X., Kivelson, S. A. & Lee, D. H. Superconductor-to-metal transition in overdoped cuprates. *npj Quantum Mater.* **6**, 36 (2021).
- <sup>19</sup> Gu, Q. et al. Directly visualizing the sign change of d-wave superconducting gap in  $\text{Bi}_2\text{Sr}_2\text{CaCu}_2\text{O}_{8+\delta}$  by phase-referenced quasiparticle interference. *Nat. Commun.* **10**, 1603 (2019).
- <sup>20</sup> Anderson, P. W. Is There Glue in Cuprate Superconductors? *Science* **316**, 1705-1707 (2007).
- <sup>21</sup> Kivelson, S. A. et al. How to detect fluctuating stripes in the high-temperature superconductors. *Rev. Mod. Phys.* **75**, 1201-1241 (2003).
- <sup>22</sup> Eduardo, H. et al. Ubiquitous Interplay Between Charge Ordering and High-Temperature Superconductivity in Cuprates. *Science* **343**, 393-396 (2014).
- <sup>23</sup> Hoffman, J. E. et al. A four unit cell periodic pattern of quasiparticle states surrounding vortex cores in  $\text{Bi}_2\text{Sr}_2\text{CaCu}_2\text{O}_{8+\delta}$ . *Science* **295**, 466-469 (2002).
- <sup>24</sup> Fischer, Ø., Kugler, M., Maggio-Aprile, I., Berthod, C. & Renner, C. Scanning tunneling spectroscopy of high-temperature superconductors. *Rev. Mod. Phys.* **79**, 353-419 (2007).
- <sup>25</sup> Damascelli, A., Hussain, Z. & Shen, Z. X. Angle-Resolved Photoemission Studies of the Cuprate Superconductors. *Rev. Mod. Phys.* **75**, 473-541 (2003).
- <sup>26</sup> Norman, M. R. et al. Destruction of the Fermi surface in underdoped high- $T_c$  superconductors. *Nature* **392**, 157-160 (1998).
- <sup>27</sup> Tranquada, J. M., et al. Neutron Diffraction from Magnetic

- Order in Superconducting  $\text{La}_{2-x}\text{Sr}_x\text{CuO}_4$ . *Nature* **375**, 561-563 (1995).
- <sup>28</sup> Keimer, B., Kivelson, S. A., Norman, M. R., Uchida, S. & Zaanen, J. From quantum matter to high-temperature superconductivity in copper oxides. *Nature* **518**, 179–186 (2015).
- <sup>29</sup> Timusk, T. & Statt, B. The pseudogap in high-temperature superconductors: an experimental survey. *Rep. Prog. Phys.* **62**, 61–122 (1999).
- <sup>30</sup> Basov, D. N. & Timusk, T. Electrodynamics of High- $T_c$  superconductors. *Rev. Mod. Phys.* **77**, 721-779 (2005).
- <sup>31</sup> Fausti, D. et al. Light-induced superconductivity in a stripe-ordered cuprate. *Science* **331**, 189-191 (2011).
- <sup>32</sup> Sachdev, S. Colloquium: Order and quantum phase transitions in the cuprate superconductors. *Rev. Mod. Phys.* **75**, 913-932 (2003).
- <sup>33</sup> Chang, J. et al. Direct observation of competition between superconductivity and charge density wave order in  $\text{YBa}_2\text{Cu}_3\text{O}_{6.67}$ . *Nat. Phys.* **8**, 871-876 (2012).
- <sup>34</sup> Comin, R. et al. Broken translational and rotational symmetry via charge stripe order in underdoped  $\text{YBa}_2\text{Cu}_3\text{O}_{6+y}$ . *Science* **343**, 390-392 (2014).
- <sup>35</sup> Aeppli, G., Mason, T. E., Hayden, S. M., Mook, H. A. & Kulda, J. Nearly singular magnetic fluctuations in the normal state of a High- $T_c$  cuprate superconductor. *Science* **278**, 1432–1435 (1997).
- <sup>36</sup> Lawler, M. J. et al. Intra-unit-cell electronic nematicity of the High- $T_c$  copper-oxide pseudogap states. *Nature* **466**, 347-351 (2010).
- <sup>37</sup> Fernandes, R. M., Chubukov, A. V. & Schmalian, J. What drives nematic order in iron-based superconductors? *Nat. Phys.* **10**, 97-104 (2014).
- <sup>38</sup> Vojta, M. Lattice symmetry breaking in cuprate superconductors: stripes, nematics, and superconductivity. *Advances in Physics* **58**, 699-820 (2009).
- <sup>39</sup> Komiya, S., Chen, H. D., Zhang, S. C., & Ando, Y. Magic doping fractions for high-temperature superconductors. *Phys. Rev. Lett.* **94**, 207004 (2005).
- <sup>40</sup> Wise, W. D. et al. Charge-density-wave origin of cuprate checkerboard visualized by scanning tunnelling microscopy. *Nat. Phys.* **4**, 696-699 (2008).
- <sup>41</sup> Chen, H.D., Vafek, O., Yazdani, A. & Zhang, S. C. Pair density wave in the pseudogap state of high temperature superconductors. *Phys. Rev. Lett.* **93**, 187002 (2004).
- <sup>42</sup> Lee, P. A., Nagaosa, N. & Wen, X. G. Doping a mott insulator: Physics of high-temperature superconductivity. *Rev. Mod. Phys.* **78**, 17-85 (2006).
- <sup>43</sup> Fradkin, E., Kivelson, S. A. & Tranquada, J. M. Colloquium: Theory of intertwined orders in high temperature superconductors. *Rev. Mod. Phys.* **87**, 457-482 (2015).
- <sup>44</sup> Emery, V. J. et al. Stripe phases in high-temperature superconductors. *Proceedings of the National Academy of Sciences* **96**, 8814-8817 (1999).
- <sup>45</sup> Salamon, M. B. & Jaime, M. (2001). The physics of manganites: Structure and transport. *Rev. Mod. Phys.* **73**, 583 (2001).
- <sup>46</sup> Scalapino, D. J. A common thread: The pairing interaction for unconventional superconductors. *Rev. Mod. Phys.* **84**, 1383 (2012).
- <sup>47</sup> Berg, E., Fradkin, E. & Kivelson, S. Charge-4e superconductivity from pair-density-wave order in certain high-temperature superconductors. *Nat. Phys.* **5**, 830–833 (2009).
- <sup>48</sup> Melikyan, A., & Tešanović, Z. Model of phase fluctuations in a lattice d-wave superconductor: Application to the Cooper-pair charge-density wave in underdoped cuprates. *Phys. Rev. B* **71**, 214511 (2005).
- <sup>49</sup> Wang, Y. et al. Real-space observation of charge ordering in epitaxial  $\text{La}_{2-x}\text{Sr}_x\text{CuO}_4$  films. *npj Quantum Mater.* **4**, 15 (2019).
- <sup>50</sup> Valla, T. et al. Evidence for Quantum Critical Behavior in the Optimally Doped Cuprate  $\text{Bi}_2\text{Sr}_2\text{CaCu}_2\text{O}_{8+\delta}$ . *Science* **285**, 2110-2113 (1999).
- <sup>51</sup> Shen, K. M. et al. Nodal quasiparticles and antinodal charge ordering in  $\text{Ca}_{2-x}\text{Na}_x\text{CuO}_2\text{Cl}_2$ . *Science* **307**, 901-904 (2005).
- <sup>52</sup> Yamada, K. et al. Doping dependence of the spatially modulated dynamical spin correlations and the superconducting-transition temperature in  $\text{La}_{2-x}\text{Sr}_x\text{CuO}_4$ . *Phys. Rev. B* **57**, 6165–6172 (1998).
- <sup>53</sup> Croft, T. P., Lester, C., Senn, M. S., Bombardi, A. & Hayden, S. M. Charge density wave fluctuations in  $\text{La}_{2-x}\text{Sr}_x\text{CuO}_4$  and their competition with superconductivity. *Phys. Rev. B* **89**, 224513 (2014).
- <sup>54</sup> Hanaguri, T. et al. A checkerboard electronic crystal state in lightly hole-doped  $\text{Ca}_{2-x}\text{Na}_x\text{CuO}_2\text{Cl}_2$ . *Nature* **430**, 1001–1005 (2004).
- <sup>55</sup> von Arx, K. et al. Fate of charge order in overdoped La-based cuprates. *npj Quantum Mater.* **8**, 7 (2023).
- <sup>56</sup> Sacépé, B. et al. Localization of preformed Cooper pairs in disordered superconductors. *Nat. Phys.* **7**, 239-244 (2011).
- <sup>57</sup> Cai, P. et al. Visualizing the evolution from the Mott insulator to a charge-ordered insulator in lightly doped cuprates. *Nat. Phys.* **12**, 1047–1051 (2016).
- <sup>58</sup> Caviglia, A. D. et al. Electric field control of the  $\text{LaAlO}_3/\text{SrTiO}_3$  interface ground state. *Nature* **456**, 624-627 (2008).
- <sup>59</sup> Li, H. et al. Low-energy gap emerging from confined nematic states in extremely underdoped cuprate superconductors. *npj Quantum Mater.* **8**, 18 (2023).
- <sup>60</sup> Imada, M., Fujimori, A. & Tokura, Y. Metal-insulator transitions. *Rev. Mod. Phys.* **70**, 1039-1263 (1998).
- <sup>61</sup> Anderson, P. W. Absence of diffusion in certain random lattices. *Phys. Rev.* **109**, 1492-1505 (1958).
- <sup>62</sup> Monthoux, P., Pines, D. & Lonzarich, G. Superconductivity without phonons. *Nature* **450**, 1177–1183 (2007).
- <sup>63</sup> Ge, J. et al. Charge-4 e and Charge-6 e Flux Quantization and Higher Charge Superconductivity in Kagome Superconductor Ring Devices. *Physical Review X* **14**, 021025 (2024).
- <sup>64</sup> Sato, T., Souma, S., Takahashi, T. & Fujimori, A. Angle-resolved photoemission study of the superconducting gap in  $\text{MgB}_2$ . *Phys. Rev. Lett.* **87**, 097003 (2001).
- <sup>65</sup> Zhang, P. et al. Observation of topological superconductivity on the surface of an iron-based superconductor. *Science* **360**, 182-186 (2018).
- <sup>66</sup> Qian, T. et al. Absence of a holelike Fermi surface for the iron-based  $\text{K}_{0.8}\text{Fe}_{1.7}\text{Se}_2$  superconductor revealed by angle-resolved photoemission spectroscopy. *Phys. Rev. Lett.* **106**, 187001 (2011).
- <sup>67</sup> Liu, D. et al. Electronic origin of high-temperature superconductivity in single-layer FeSe superconductor. *Nat. Commun.* **3**, 931-936 (2012).
- <sup>68</sup> Wang, D. Evidence for Majorana bound states in an iron-based superconductor. *Science* **362**, 333-335 (2018).
- <sup>69</sup> Ding, H. et al. Observation of Fermi-Surface-Dependent Nodeless Superconducting Gaps in  $\text{Ba}_{0.6}\text{K}_{0.4}\text{Fe}_2\text{As}_2$ . *EPL* **83**, 47001-47006 (2008).
- <sup>70</sup> Zhang, Y. et al. Nodeless Superconducting Gap in  $\text{A}_x\text{Fe}_2\text{Se}_2$  (A = K, Cs) Revealed by Angle-Resolved Photoemission Spectroscopy. *Nat. Mater.* **10**, 273-277 (2011).
- <sup>71</sup> Thurston, T. R. et al. Neutron scattering study of the magnetic excitations in metallic and superconducting  $\text{La}_{2-x}\text{Sr}_x\text{CuO}_{4-y}$ .

- Phys. Rev. B* **40**, 4585 (1989).
- <sup>72</sup> Rossat-Mignod, J. et al. Neutron scattering study of the  $\text{YBa}_2\text{Cu}_3\text{O}_{6+x}$  system. *Physica C: Superconductivity* **185**, 86-92 (1991).
- <sup>73</sup> Lee, Y. S. et al. Neutron-scattering study of spin-density wave order in the superconducting state of excess-oxygen-doped  $\text{La}_2\text{CuO}_{4+y}$ . *Phys. Rev. B* **60**, 3643 (1999).
- <sup>74</sup> Meissner, W. & Ochsenfeld, R. Ein neuer effekt bei eintritt der supraleitfähigkeit. *Naturwissenschaften* **21**, 787-788 (1933).
- <sup>75</sup> Mattis, Daniel C. The theory of magnetism I: Statics and Dynamics. Vol. 17. Springer Science & Business Media (2012).
- <sup>76</sup> Drude, Paul. Zur elektronentheorie der metalle. *Annalen der Physik* **312**, 687-692 (1902).
- <sup>77</sup> Hubbard, J. Electron correlations in narrow energy bands. *Proc. Roy. Soc.* **276**, 238-257 (1963).
- <sup>78</sup> Anderson, P. W. More Is Different: Broken symmetry and the nature of the hierarchical structure of science. *Science* **177**, 393-396 (1972).
- <sup>79</sup> Uhlenbeck, G. E. & Goudsmit, S. Ersetzung der Hypothese vom unmechanischen Zwang durch eine Forderung bezüglich des Inneren Verhaltens jedes einzelnen Elektrons. *Nature* **117**, 264-265 (1926).
- <sup>80</sup> Dirac, P. A. M. Quantised Singularities in the Electromagnetic Field. *Proc. Roy. Soc. A* **133**, 60-72 (1931).
- <sup>81</sup> Ginzburg, V. L. & Landau, L. D. On the Theory of Superconductivity. *Zh. Eksp. Teor. Fiz.* **20**, 1064-1082 (1950).
- <sup>82</sup> Planck, M. Zur theorie des gesetzes der energieverteilung im normal spectrum. *Verh. Dtsch. Phys. Ges.* **2**, 237-245 (1900).
- <sup>83</sup> He, Y. et al. Superconducting Fluctuations in Overdoped  $\text{Bi}_2\text{Sr}_2\text{CaCu}_2\text{O}_{8+\delta}$ . *Phys. Rev. X* **11**, 031068 (2021).
- <sup>84</sup> Yao, H., Tsai, W. F., & Kivelson, S. A. Myriad phases of the checkerboard Hubbard model. *Phys. Rev. B* **76**, 161104 (2007).
- <sup>85</sup> Patterson, C. H. Small polarons and magnetic antiphase boundaries in  $\text{Ca}_{2-x}\text{Na}_x\text{CuO}_2\text{Cl}_2$  ( $x=0.06, 0.12$ ): Origin of striped phases in cuprates. *Phys. Rev. B* **77**, 094523 (2008).
- <sup>86</sup> Chadov, S. et al. Electronic structure, localization, and spin-state transition in Cu-substituted FeSe:  $\text{Fe}_{1-x}\text{Cu}_x\text{Se}$ . *Phys. Rev. B* **81**, 104523 (2010).
- <sup>87</sup> Shen, K. M. et al. Nodal Quasiparticles and Antinodal Charge Ordering in  $\text{Ca}_{2-x}\text{Na}_x\text{CuO}_2\text{Cl}_2$ . *Science* **307**, 901-904 (2005).
- <sup>88</sup> Yang, H.-B. et al. Emergence of Competing Order and Unusual Low-Energy Excitations in Superconducting  $\text{La}_{2-x}\text{Sr}_x\text{CuO}_4$ . *Nature* **456**, 77-80 (2008).
- <sup>89</sup> Sun H. L. et al. Signatures of superconductivity near 80 K in a nickelate under high pressure. *Nature* **621**, 493-498 (2023).
- <sup>90</sup> Geisler, B. et al. Structural transitions, octahedral rotations, and electronic properties of  $\text{A}_3\text{Ni}_2\text{O}_7$  rare-earth nickelates under high pressure. *npj Quantum Mater.* **9**, 38 (2024).
- <sup>91</sup> Ai, P. et al. Observation of Superconductivity at 38 K in  $(\text{Li, Fe})\text{OHFeSe}$ . *Chin. Phys. Lett.* **36**, 067402-067404 (2019).
- <sup>92</sup> Feng, D. L. et al. Electronic structure of the trilayer cuprate superconductor  $\text{Bi}_2\text{Sr}_2\text{Ca}_2\text{Cu}_3\text{O}_{10+\delta}$ . *Phys. Rev. Lett.* **88**, 107001 (2002).
- <sup>93</sup> Matsui, H. et al. BCS-like Bogoliubov quasiparticles in high- $T_c$  superconductors observed by angle-resolved photoemission spectroscopy. *Phys. Rev. Lett.* **90**, 217002 (2003).
- <sup>94</sup> Kunisada, S. et al. Observation of Bogoliubov band hybridization in the optimally doped trilayer  $\text{Bi}_2\text{Sr}_2\text{Ca}_2\text{Cu}_3\text{O}_{10+\delta}$ . *Phys. Rev. Lett.* **119**, 217001 (2017).
- <sup>95</sup> Ideta, S. et al. Hybridization of Bogoliubov quasiparticles between adjacent  $\text{CuO}_2$  layers in the triple-layer cuprate  $\text{Bi}_2\text{Sr}_2\text{Ca}_2\text{Cu}_3\text{O}_{10+\delta}$  studied by angle-resolved photoemission spectroscopy. *Phys. Rev. Lett.* **127**, 217004 (2021).
- <sup>96</sup> Luo, X. et al. Electronic origin of high superconducting critical temperature in trilayer cuprates. *Nat. Phys.* **19**, 1841-1847 (2023).
- <sup>97</sup> Fujii, T., Terasaki, I., Watanabe, T. & Matsuda, A. Doping dependence of anisotropic resistivities in the trilayered superconductor  $\text{Bi}_2\text{Sr}_2\text{Ca}_2\text{Cu}_3\text{O}_{10+\delta}$ . *Phys. Rev. B* **66**, 024507 (2002).
- <sup>98</sup> Kordyuk, A. A. Electronic Structure and Collective Modes in Fe-Based Superconductors. *Low Temp. Phys.* **38**, 888-898 (2012).
- <sup>99</sup> Hirschfeld, P. J., Korshunov, M. M. & Mazin, I. I. Gap symmetry and structure of Fe-based superconductors. *Reports on Progress in Physics* **74**, 124508 (2011).
- <sup>100</sup> Chubukov, A. V., Efremov, D. V. & Eremin, I. Magnetism, superconductivity, and pairing symmetry in iron-based superconductors. *Phys. Rev. B* **78**, 134512 (2008).
- <sup>101</sup> Du, Z. et al. Scrutinizing the double superconducting gaps and strong coupling pairing in  $(\text{Li}_{1-x}\text{Fe}_x)\text{OHFeSe}$ . *Nat. Commun.* **7**, 10565 (2016).
- <sup>102</sup> Lee, C. et al. Relationship between crystal structure and superconductivity in iron-based superconductors. *Solid State Commun.* **152**, 644-648 (2012).
- <sup>103</sup> Hansen, M.F. et al. Superconductivity in the crystallogenic  $\text{LaFeSiO}_{1-\delta}$  with squeezed FeSi layers. *npj Quantum Mater.* **7**, 86 (2022).
- <sup>104</sup> Gao, L. et al. Superconductivity up to 164 K in  $\text{HgBa}_2\text{Ca}_{m-1}\text{Cu}_m\text{O}_{2m+2+\delta}$  ( $m=1, 2, \text{ and } 3$ ) under quasi-hydrostatic pressures. *Phys. Rev. B* **50**, 4260-4263 (1994).
- <sup>105</sup> Sun, L. et al. Momentum-Dependent Electron Dynamics and Spin-Fluctuation-Driven Superconductivity in  $\text{FeSe}_{0.45}\text{Te}_{0.55}$ . *Nature* **483**, 67-70 (2012).
- <sup>106</sup> Tafti, F. F. et al. Superconductivity in the Vicinity of Antiferromagnetic Order in CrAs. *Nat. Phys.* **9**, 349-354 (2013).
- <sup>107</sup> Wu, D. S. et al. Interplay between Superconductivity and Magnetic Order in  $\text{CeCoIn}_5$ . *Phys. Rev. B* **101**, 224508-224514 (2020).
- <sup>108</sup> Xie, T. et al. Direct Determination of the Superconducting Gap in Heavy Fermion  $\text{CeCoIn}_5$  by Quasiparticle Interference. *Phys. Rev. Lett.* **120**, 267003-267008 (2018).
- <sup>109</sup> Kim, C. et al. Observation of Anisotropic Gap in the Superconducting State of  $\text{YBa}_2\text{Cu}_3\text{O}_{7-\delta}$ . *Phys. Rev. Lett.* **77**, 4054-4057 (1996).
- <sup>110</sup> Hirsch, J. E. BCS theory of superconductivity: it is time to question its validity. *Physica Scripta* **80**, 035702 (2009).
- <sup>111</sup> [https://www.reddit.com/r/gifs/comments/1q0d8n/the\\_meissner\\_effect/](https://www.reddit.com/r/gifs/comments/1q0d8n/the_meissner_effect/)
- <sup>112</sup> London, F. & London, H. The electromagnetic equations of the supraconductor. *Proc. Roy. Soc.* **149**, 71-88 (1935).